Electrochimica Acta 393 (2021) 139045

Contents lists available at ScienceDirect

Electrochimica Acta

journal homepage: www.elsevier.com/locate/electacta

Tensorial effective transport properties of Li-ion battery separators elucidated by computational multiscale modeling

Mingzhao Zhuo[a,*], Davide Grazioli[b], Angelo Simone[a,b]

[a] Faculty of Civil Engineering and Geosciences, Delft University of Technology, Delft, The Netherlands
[b] Department of Industrial Engineering, University of Padova, Padua, Italy

ARTICLE INFO

Article history:
Received 24 May 2021
Revised 24 July 2021
Accepted 2 August 2021
Available online 12 August 2021

Keywords:
Multiscale battery component modeling
Computational homogenization
Ionic transport in lithium ion battery separators
Concentration-dependent transport property
Time-evolving microstructure

ABSTRACT

Existing battery modeling works have limitations in addressing the dependence of transport properties on local field variations and characterizing the response of anisotropic media. These limitations are tackled by means of a nested finite element (FE^2) multiscale framework in which microscale simulations are employed to comprehensively characterize an anisotropic medium (macroscale). The approach is applied to the numerical simulation of transport processes in lithium ion battery separators. From the microscale solution, homogenized fluxes and their dependence on the downscaled macroscale variables are upscaled, thereby replacing otherwise assumed macroscale constitutive laws. The tensorial nature of macroscale effective transport properties stems from the numerical treatment. The proposed approach is verified against full-scale simulations. Several numerical examples are used to demonstrate the perils associated with accepted procedures, leading in some cases to severe discrepancies in the prediction of field quantities (from differences in the potential drop across the separator of about 27% for a fixed microstructure to more than 100% in the case of an evolving microstructure). Despite the use of simplified assumptions (e.g., synthetic microstructures), the numerical results demonstrate the importance of a tensorial description of transport properties in the modeling of battery processes.

1. Introduction

Electrochemical models employed for battery cell performance prediction are based upon assumptions that are functional to their efficient numerical solution. A common assumption is that transport properties are constant when calculating the effective transport coefficients. Moreover, the effective transport properties are usually represented by a scalar or, at best, by a tensor with null cross-terms. The implication of this choice is that the role of the microstructure is not fully reflected by the effective transport properties. This paper discusses these aspects by means of a nested finite element (FE^2) multiscale framework endowed with nonlinear physics-based constitutive models at the microscale (pore-scale) and well-defined information exchange between micro- and macro-scales (cell level).

The popular DFN model [1], also referred to as the pseudo two-dimensional (P2D) model, describes porous battery cell components as homogenized macroscopic continua using averaged mass and charge transport equations. The impact of a component's microstructure on the overall response is taken into account by means of effective transport properties. These parameters are identified either through Bruggeman relationship [2], or through sets of simulations independently performed on microstructural volume elements. Although the direct application of the first approach is straightforward, its accuracy in terms of battery response prediction is limited [3,4]. For this reason, variants of Bruggeman relationship are available in the literature and are tuned through experimental investigations on a problem-specific basis [5] (an example of such an approach relevant for lithium ion battery separators is represented by Cannarella and Arnold [6]). The second approach reaches a compromise between computational cost and a microstructure-informed analysis. This compromise is reached through a simple multiscale computational strategy [3,7–9] in which the macroscale formulation is analogous to that of the DFN model as summarized in Sec 3.1.

Some problems however arise with the second approach. First, the coupling between mass and charge transport is disregarded

* Corresponding author.
E-mail addresses: m.zhuo@tudelft.nl, mzhuo@connect.ust.hk, m.zhuo@tudelft.nl (M. Zhuo), davide.grazioli@unipd.it (D. Grazioli), angelo.simone@unipd.it, a.simone@tudelft.nl (A. Simone).
URL: https://orcid.org/0000-0003-2495-1508 (D. Grazioli), https://orcid.org/0000-0001-9726-0068 (A. Simone)

https://doi.org/10.1016/j.electacta.2021.139045

Nomenclature

c_e	concentration at the pore-scale
$\langle c_m \rangle_e$	intrinsic volume average of microscale concentrationy
c_h	homogenized concentration
c_m	concentration at the microscale
$\tilde{c}_m$	microscale concentration fluctuation field
$\langle c_m \rangle_e$	intrinsic volume averages of microscale concentration
c_M	concentration at the macroscale
f_e	mean molar activity coefficient
I_{app}	applied current
$\mathbf{i}_e$	pore-scale current density
$\mathbf{i}_m$	microscale current density
$\mathbf{i}_M$	macroscale current density (averaged flux)
$\mathbf{n}_{ex}$	outward unit normal vector to RVE boundary Γ_{ex}
$\mathbf{q}_e$	pore-scale lithium ion flux
$\mathbf{q}_m$	microscale lithium ion flux
$\mathbf{q}_M$	macroscale lithium ion flux (averaged flux)
t	time
t_e	transference number
t_{end}	end of simulation time
$\mathbf{x}$	point in RVE
$\mathbf{x}_r$	reference point in RVE
D_e	bulk diffusivity
D_{eff}	effective bulk diffusivity
D_{ref}	bulk diffusivity at concentration $c_e = 1.0\text{mol/L}$
$\mathbf{D}_{eff}$	macroscale diffusivity tensor
F	Faraday constant
$\mathbf{K}_q$, $\mathbf{K}_i$	consistent tangents summarizing the (numerical) relationships between inputs ($\mathbf{X}$) and outputs ($\mathbf{q}_M$ and $\mathbf{i}_M$) of the microscale simulations
R	gas constant
T	absolute temperature
V_e	electrolyte domain
V_b	ion-transport blocking phase domain
$\mathbf{X}$	vector containing macroscale concentration and potential fields and their gradients
α	Bruggeman exponent
δ	effective transport coefficient
$\boldsymbol{\delta}$	tensor of the effective transport coefficients
δ_{ij}	effective transport coefficients in $\boldsymbol{\delta}$
ϵ	electrolyte volume fraction (i.e., RVE porosity)
κ_D	diffusional conductivity
$\kappa_{D,eff}$	effective diffusional conductivity
κ_e	bulk conductivity
κ_{eff}	effective bulk conductivity
κ_{ref}	bulk conductivity at concentration $c_e = 1.0\text{mol/L}$
τ	tortuosity
ϕ_e	electric potential at the pore-scale
ϕ_h	homogenized electric potential
ϕ_m	electric potential at the microscale
ϕ_M	electric potential at the macroscale
$\tilde{\phi}_m$	microscale potential fluctuation field
$\langle \phi_m \rangle_e$	intrinsic volume averages of microscale potential
Γ_{eb}	interface between electrolyte and ion-transport blocking phase
Γ_{ex}	RVE boundary
$\Gamma_{e_{ex}}$	RVE boundary associated to the electrolyte
$\Gamma_{b_{ex}}$	RVE boundary associated to the ion-transport blocking phase
$\Delta\phi$	potential drop
$\nabla \cdot \boldsymbol{f}$	divergence of vector field $\boldsymbol{f}$
∇	gradient operator

when a simulation is performed on the microstructure volume element. Second, microscale simulations are performed with a constant bulk transport property. The omission of the concentration dependence leads to the question of whether we can safely use the same concentration dependence function for the effective transport properties at the macroscale (this aspect is discussed in Sec 3.1.1). Finally, the dimensionality of the effective properties is understood differently. Some authors [3,7,8] treat effective properties as scalar. Others [4,5,9–12] report different properties in through-plane and in-plane directions (i.e., the direction of transport between electrodes and those directions orthogonal to it [9], respectively), but do not make reference to cross-terms (effective transport coefficients that describe the occurrence of flux in one direction when a gradient of the field variable is applied in the orthogonal direction). Cooper et al. [4] suggest to describe local heterogeneities in the microstructure using a vectorial tortuosity. Even if this treatment is unconditionally applicable to isotropic media, it is not necessarily adequate for porous battery components. In fact, experimental evidence indicates that transport properties in battery electrodes are sensitive to the direction of the applied gradient [5,10]. A tensorial description thus appears more adequate [13–16]. Furthermore, as the battery components morphology changes with electrochemical cycling (due, for example, to the deformations of constituents [17]), initially isotropic porous structures might not remain isotropic during battery operations.

Single-scale simulations (also referred to as direct numerical simulations) fully resolve the microstructure [18–20] and can be employed to address some of the issues illustrated above. However, a detailed numerical representation of porous battery components (up to their microstructure) requires a significant computational effort, especially when the pore/particle size is two to three orders of magnitude smaller than the typical size of a battery cell [4,21]. Direct microstructure-resolved approaches are computationally expensive and are therefore deemed unsuitable for battery performance improvements through model-instructed microstructure manipulation if an entire battery cell is considered and in the case of performance optimization studies.

To address the limitations just described, we propose the use of a FE^2-based computational homogenization scheme and present a proof-of-concept two-scale framework with simple information exchange between macro- and micro-scale levels. The approach is also used to extract effective properties as a by-product of the numerical procedure as discussed in Sec 3.1.2. Although the FE^2 approach has been successfully applied to many problems, ranging from mechanical equilibrium [22–24] and transport [25] problems to multi-physics problems [26–29], the analyses reported in this manuscript have been performed on academic, yet plausible, examples for the sake of verification of the framework. Its application to engineering-relevant problems does however require the use of ad-hoc procedures [30,31].

The theoretical framework of a computational homogenization approach for battery applications has been recently developed by Salvadori et al. [32,33] to account for the multi-physics nature of processes taking place in battery cells, including diffusion, migration, intercalation, and mechanics. In this paper, we present an alternative FE^2 framework focused on ionic transport through porous battery cell separators (Sec 2). In the separator only two constituents coexist: a liquid electrolyte filling the pores of an inert and electrochemically inactive membrane (e.g., polyolefin [9]). The absence of active materials results in significant modeling simplifications, as no lithium exchange occurs between the constituents.

This allows capturing the most fundamental phenomena and assess the applicability of the FE^2 method to the battery setting.

Battery cell separators can have a macroscopically anisotropic response [9,12] and undergo deformation during battery cycling (as a result of either electrode deformations [34] or externally applied mechanical loads [6]), just like any other battery component. The design of the separator is not secondary to that of electrodes, as experimental and numerical investigations indicate that it is the transport-limiting component of a cell when subject to deformations [6,9]. We thus employ the proposed multiscale framework to simulate charge processes and focus on the battery separator response. For simplicity, we consider two-dimensional (2-D) microstructures only and do not discuss procedures [30,31] to reduce the simulation costs of the FE^2 approach. In Sec 3 the features of the FE^2 approach are discussed in the light of the limitations of existing models, under conditions that allow also simpler approaches to be examined in Sec 3.3. Furthermore, we perform simulations of battery separators both with single-scale (microstructure-resolved) and FE^2 approaches and show that the same level of accuracy is achieved (Sec 3.2), thus verifying our approach. Finally, Sec 3.4 demonstrates the potential of the approach to describe the consequences of different microstructure deformation paths of a separator during the charge process. The results show that alteration of the microstructure morphology alone (i.e., at constant porosity) results in a significant alteration of the macroscopic response of the system.

2. Multiscale approach

Next, the FE^2 approach employed in this study is summarized, and the governing equations at the two scales together with the corresponding information-passing procedures are reported. Details about the numerical implementation are provided in Sec S4 in the Supplementary Material (SM). In the remainder of the paper, quantities at the microscale and macroscale are identified by subscripts 'm' and 'M', respectively.

2.1. Macroscale model

We restrict our scope to ionic transport through the battery cell separator where there is no mutual interfacial flux between electrolyte and porous membrane. A schematic of the problem is reported in Fig. 1a. The ionic transport in the electrolyte is governed by mass conservation of lithium ions and electric charge balance, expressed as

$$\epsilon \frac{\partial c_\mathrm{M}}{\partial t} + \nabla \cdot \mathbf{q}_\mathrm{M} = 0 \quad \text{and} \tag{1a}$$

$$\nabla \cdot \mathbf{i}_\mathrm{M} = 0 \quad \text{in} \quad \Omega \times (0, t_\mathrm{end}), \tag{1b}$$

respectively, where ϵ is the electrolyte volume fraction (i.e., the membrane porosity), $\mathbf{q}_\mathrm{M}$ is the lithium ion flux, $\mathbf{i}_\mathrm{M}$ is the current density, and c_M represents the macroscale concentration. The macroscale governing equations can be derived through a volume-averaging approach applied to the single scale governing equations as shown in Sec S3 in the SM.

Equation (1) expresses the macroscale balance equations over the homogenized domain Ω (Fig. 1b). It is remarked that macroscale concentration c_M and potential ϕ_M (not explicitly present in Eq. (1b)) are the two field variables to solve for, and that the macroscale constitutive relations for $\mathbf{q}_\mathrm{M}$ and $\mathbf{i}_\mathrm{M}$ are numerically obtained through the information exchange between the two scales (Sec 2.4). As schematically depicted in Fig. 1, the macroscale solution fields c_M and ϕ_M and their gradients are downscaled to the microscale problem, and the macroscale fluxes and their tangents are evaluated from the microscale solution and upscaled to the macroscale problem. Initial and boundary conditions complete the macroscale problem definition and are provided in Sec 3 for each example considered.

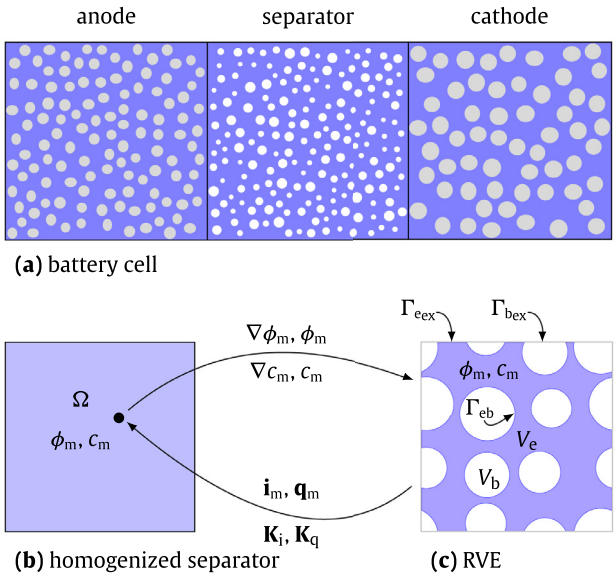

Fig. 1. Schematic of the multiscale approach showing (a) a battery cell with porous anode, separator, and cathode (the porous electrode and separator domains are filled with the electrolyte occupying domain V_e), (b) the homogenized domain at the macroscale, and (c) a microscopic representative volume element (RVE) of battery separator, consisting of blue-shaded electrolyte domain V_e and gray-shaded ion-transport blocking phase domain V_b. The blocking phases represent the separator membrane. The information exchange between macro- and micro-scales is depicted in panels (b) and (c). The potential (ϕ_M) and its gradient ($\nabla\phi_M$), and the concentration (c_M) and its gradient (∇c_M) at a point of the macroscale domain Ω (integration point in the context of FEM) are transferred to the microscale to define the boundary conditions, while the averaged fluxes ($\mathbf{i}_M$, $\mathbf{q}_M$) and their dependence ($\mathbf{K}_i$, $\mathbf{K}_q$) on the downscaled quantities are transferred back after the microscale quantities (ϕ_m and c_m) are evaluated. The RVE boundary Γ_{ex} is divided into two parts, each associated with a phase, such that $\Gamma_{ex} = \Gamma_{e_{ex}} \cup \Gamma_{b_{ex}}$ with $\Gamma_{e_{ex}} \cap \Gamma_{b_{ex}} = \varnothing$.

2.2. Downscaling

The boundary conditions enforced at the microscale level are obtained by downscaling macroscale quantities at each integration point of the macroscale mesh: concentration c_M, potential ϕ_M, and their gradients ∇c_M and $\nabla\phi_\mathrm{M}$, respectively. For conciseness, these quantities are stacked in the column vector

$$\mathbf{X} = \left[\left(\nabla c_\mathrm{M}\right)^\mathrm{T} \quad c_\mathrm{M} \quad \left(\nabla \phi_\mathrm{M}\right)^\mathrm{T} \quad \phi_\mathrm{M} \right]^\mathrm{T}. \tag{2}$$

2.3. Microscale model

The microscale problem is defined on a representative volume element (RVE), as shown in Fig. 1c, associated to a macroscale integration point of the homogenized separator (Fig. 1b). The balance equations at the microscale, analogously to those used at the macroscale (Eq. (1)), are expressed as

$$\nabla \cdot \mathbf{q}_\mathrm{m} = 0 \quad \text{and} \tag{3a}$$

$$\nabla \cdot \mathbf{i}_\mathrm{m} = 0 \quad \text{in} \quad V_\mathrm{e}, \tag{3b}$$

where V_e is the electrolyte domain bounded by $\Gamma_{e_{ex}} \cup \Gamma_{eb}$ with $\Gamma_{e_{ex}} \cap \Gamma_{eb} = \varnothing$ (Fig. 1c). Subscripts 'e' and 'b' refer to electrolyte and ion-transport blocking phase (porous membrane), respectively. The ion-transport blocking phase is not modeled because no transport processes occur within it (in this study the blocking phase is

merely an obstacle that is impenetrable to ions). At the microscale we neglect the time variation of the concentration field assuming that the RVE is sufficiently small to allow the steady state configuration to be suddenly attained. This condition is met in battery separators where the characteristic size of the pores is orders of magnitude smaller than the typical thickness of porous membranes [21] (a discussion is provided in Sec S8 of the SM). We remark that simulations of porous battery electrodes within a FE^2 framework might call for a concurrent time modeling between macroscale and microscale, as discussed by Salvadori et al. [33]. Indeed, diffusion in active material can be so slow that the time evolution of microscale fields becomes comparable to that of the macroscale counterparts. The low diffusivity of the active materials is indeed recognized as one of the limiting factor towards the full exploitation of the theoretical battery energy over a range of operating conditions, as the thorough investigation performed by Du et al. [35] demonstrates.

Constitutive equations are explicitly provided at this scale, where the ionic transport processes is modeled through the concentrated solution theory [1]. The lithium ion flux, and the current density read

$$\mathbf{q}_\mathrm{m} = -D_\mathrm{e}\,\boldsymbol{\nabla} c_\mathrm{m} + \frac{t_\mathrm{e}}{F}\,\mathbf{i}_\mathrm{m}, \tag{4a}$$

and

$$\mathbf{i}_\mathrm{m} = -\kappa_\mathrm{e}\,\boldsymbol{\nabla}\phi_\mathrm{m} + \kappa_\mathrm{D}\,\boldsymbol{\nabla}\ln c_\mathrm{m}, \tag{4b}$$

respectively, with the diffusional conductivity defined as

$$\kappa_\mathrm{D} = \frac{2RT\kappa_\mathrm{e}}{F}\left(1 + \frac{\partial \ln f_\mathrm{e}}{\partial \ln c_\mathrm{e}}\right)(1 - t_\mathrm{e}). \tag{4c}$$

The coupled set of differential Eq. (3) is solved in terms of lithium ion concentration c_m and electric potential ϕ_m. In the above equations, D_e and κ_e denote bulk diffusivity and ionic conductivity (i.e., quantities actually related to the material), respectively, t_e is the transference number, and f_e is the mean molar activity coefficient. Finally, F, R, and T represent the Faraday constant, the gas constant, and the absolute temperature, respectively.

Next, we derive the microscale boundary conditions from the macroscale quantities $\mathbf{X}$ in Eq. (2). Without loss of generality, microscale fields can be decomposed into linear contributions consistent with macroscale quantities (c_M, ϕ_M, and their gradients) and fluctuation fields $\tilde{c}_\mathrm{m}$ and $\tilde{\phi}_\mathrm{m}$ as in

$$c_\mathrm{m} = c_\mathrm{M} + \boldsymbol{\nabla} c_\mathrm{M}\cdot(\mathbf{x} - \mathbf{x}_\mathrm{r}) + \tilde{c}_\mathrm{m}, \tag{5a}$$

$$\phi_\mathrm{m} = \phi_\mathrm{M} + \boldsymbol{\nabla}\phi_\mathrm{M}\cdot(\mathbf{x} - \mathbf{x}_\mathrm{r}) + \tilde{\phi}_\mathrm{m}, \tag{5b}$$

where $\mathbf{x}$ and $\mathbf{x}_\mathrm{r}$ denote the spatial coordinates of a point and a reference point in the RVE domain, respectively.

To design the boundary conditions of the microscale problem, we assume that the volume average of the gradients of microscale variables over the whole RVE is equal to the corresponding macroscale gradients in analogy with the kinematical averaging relation used in solid mechanics to establish the macro-to-micro coupling:

$$\frac{1}{V}\int_V \boldsymbol{\nabla} c_\mathrm{m}\,\mathrm{d}V = \boldsymbol{\nabla} c_\mathrm{M}, \tag{6a}$$

$$\frac{1}{V}\int_V \boldsymbol{\nabla}\phi_\mathrm{m}\,\mathrm{d}V = \boldsymbol{\nabla}\phi_\mathrm{M}, \tag{6b}$$

where the RVE volume V is such that $V = V_\mathrm{e}\cup V_\mathrm{b}$ with $V_\mathrm{e}\cap V_\mathrm{b} = \varnothing$. The electrolyte volume fraction can thus be explicitly defined as $\epsilon = V_\mathrm{e}/V$. Note that by analogy with the problem of a RVE with holes under mechanical loading [36], the domain of the ion-transport blocking phase needs to be included in the averages (6) because the RVE is considered as a macroscale point as a whole. Substituting Eq. (5a) into the left-hand side of Eq. (6a) yields

$$\frac{1}{V}\int_V \boldsymbol{\nabla} c_\mathrm{m}\,\mathrm{d}V = \boldsymbol{\nabla} c_\mathrm{M} + \frac{1}{V}\int_V \boldsymbol{\nabla}\tilde{c}_\mathrm{m}\,\mathrm{d}V. \tag{7}$$

According to the divergence theorem, the second term in the right-hand side of Eq. (7) can be reformulated as

$$\frac{1}{V}\int_V \boldsymbol{\nabla}\tilde{c}_\mathrm{m}\,\mathrm{d}V = \frac{1}{V}\int_{\Gamma_\mathrm{ex}} \tilde{c}_\mathrm{m}\,\mathbf{n}_\mathrm{ex}\,\mathrm{d}\Gamma, \tag{8}$$

where Γ_ex is the RVE boundary (Fig. 1c). Comparing Eq. (7) with Eq. (6a) and considering Eq. (8) lead to

$$\int_{\Gamma_\mathrm{ex}} \tilde{c}_\mathrm{m}\,\mathbf{n}_\mathrm{ex}\,\mathrm{d}\,\Gamma = 0 \quad \text{and} \tag{9a}$$

$$\int_{\Gamma_\mathrm{ex}} \tilde{\phi}_\mathrm{m}\,\mathbf{n}_\mathrm{ex}\,\mathrm{d}\,\Gamma = 0, \tag{9b}$$

where the relation for ϕ_m has been obtained by analogy. Although constraint (9) can be satisfied through different sets of boundary conditions, we employ periodic boundary conditions according to Ref. [37] as discussed in Sec S2 in the SM. To uniquely solve the microscale problem, we impose two additional conditions: the intrinsic volume averages of microscale variables, as defined in Sec S1 in the SM, are set equal to the corresponding macroscale quantities:

$$\langle c_\mathrm{m}\rangle_\mathrm{e} = c_\mathrm{M}, \quad \langle\phi_\mathrm{m}\rangle_\mathrm{e} = \phi_\mathrm{M}. \tag{10}$$

A substantial difference exists between the above constraints. While the former (conservation of mass between macro- and micro-scales) must be enforced because the microscale solution depends on the actual concentration value (the material properties in Eq. (4) are concentration-dependent), the latter is enforced for consistency and is not essential provided the uniqueness of the solution is ensured.

2.4. Upscaling

In this section we describe how the homogenized quantities, based on the microscale solution and needed in the macroscale computation (Fig. 1b), are upscaled. In a continuum mechanics context it is customary to derive the micro-to-macro transition by enforcing either energy [38] (Hill-Mandel condition) or entropy [39] consistency across scales. An extended version of the Hill–Mandel condition tailored for battery cell modeling was proposed by Salvadori et al. [32,33], who equated 'the microscopic volume average of the virtual power on the RVE and the point-wise one at the macroscale' [32]. An alternative strategy is used here: we enforce

$$\frac{1}{V}\int_V \boldsymbol{\nabla} c_\mathrm{m}\cdot\mathbf{q}_\mathrm{m}\,\mathrm{d}V = \boldsymbol{\nabla} c_\mathrm{M}\cdot\mathbf{q}_\mathrm{M}, \tag{11a}$$

$$\frac{1}{V}\int_V \boldsymbol{\nabla}\phi_\mathrm{m}\cdot\mathbf{i}_\mathrm{m}\,\mathrm{d}V = \boldsymbol{\nabla}\phi_\mathrm{M}\cdot\mathbf{i}_\mathrm{M}. \tag{11b}$$

This approach presents similarities with the works of Keip, Steinmann, and Schröder [26–28] and Lee and Sundararaghavan [29]. The former focuses on the electromechanical coupling in piezoelectric and electro-active materials at multiple scales, and the authors considered the mechanical and electrical contributions independently in the scale transitions. The latter makes use of restriction (11a) to identify the micro-to-macro scale transitions for the mass flux in the context of diffusion-reaction-induced degradation of composites. Numerical evidence reported

in Sec 3.2 indicates that the micro-to-macro scale transitions obtained from Eq. (11) (given in Eq. (14)) are sound for the class of problems considered in this study.

Macroscale fluxes are obtained by following the procedure described below. By making use of Eq. (3) and the divergence theorem, the left-hand side of Eq. (11a) is expressed as

$$\frac{1}{V}\int_V \nabla c_\mathrm{m}\cdot\mathbf{q}_\mathrm{m}\,\mathrm{d}V = \frac{1}{V}\int_V \nabla\cdot(c_\mathrm{m}\,\mathbf{q}_\mathrm{m})\,\mathrm{d}V = \frac{1}{V}\int_{\Gamma_\mathrm{ex}} c_\mathrm{m}\,\mathbf{q}_\mathrm{m}\cdot\mathbf{n}_\mathrm{ex}\mathrm{d}\Gamma. \tag{12}$$

Due to the adoption of periodic boundary conditions (S.5), the term $\mathbf{q}_\mathrm{m}\cdot\mathbf{n}_\mathrm{ex}$ takes opposite value on opposite edges. This term is referred to as the anti-periodic normal flux boundary condition [37]; such a meaning can be clearly inferred from the use of Lagrange multipliers to enforce periodic boundary conditions in the microscale FE implementation discussed in Sec S.5 in the SM. Considering mass conservation Eq. (3a), periodic boundary conditions S.6, and the anti-periodic normal flux leads to (refer, e.g., to Ref. [37] for derivation details)

$$\frac{1}{V}\int_{\Gamma_\mathrm{ex}} c_\mathrm{m}\,\mathbf{q}_\mathrm{m}\cdot\mathbf{n}_\mathrm{ex}\,\mathrm{d}\Gamma = \nabla c_\mathrm{M}\cdot\frac{1}{V}\int_{\Gamma_\mathrm{ex}}\mathbf{x}\,\mathbf{q}_\mathrm{m}\cdot\mathbf{n}_\mathrm{ex}\,\mathrm{d}\Gamma. \tag{13}$$

Comparing Eq. (13) with Eqs. (11a) and (12) we obtain

$$\mathbf{q}_\mathrm{M} = \frac{1}{V}\int_{\Gamma_\mathrm{ex}}\mathbf{x}\,\mathbf{q}_\mathrm{m}\cdot\mathbf{n}_\mathrm{ex}\,\mathrm{d}\Gamma. \tag{14a}$$

An analogous procedure leads to the definition of the macroscale current density

$$\mathbf{i}_\mathrm{M} = \frac{1}{V}\int_{\Gamma_\mathrm{ex}}\mathbf{x}\,\mathbf{i}_\mathrm{m}\cdot\mathbf{n}_\mathrm{ex}\,\mathrm{d}\Gamma. \tag{14b}$$

The consistent tangents

$$\mathbf{K}_\mathrm{q} = \frac{\delta\mathbf{q}_\mathrm{M}}{\delta\mathbf{X}} \quad\text{and}\quad \mathbf{K}_\mathrm{i} = \frac{\delta\mathbf{i}_\mathrm{M}}{\delta\mathbf{X}} \tag{15}$$

are matrices that summarize the (numerical) relationships between inputs ($\mathbf{X}$) and outputs ($\mathbf{q}_\mathrm{M}$ and $\mathbf{i}_\mathrm{M}$) of the microscale simulations. Terms $\mathbf{K}_\mathrm{q}$ and $\mathbf{K}_\mathrm{i}$ are determined according to the procedure described in Sec S4.3 in the SM.

2.5. FE^2 procedure summary

In the FE^2 framework, nested finite element simulations are performed, and a microscale numerical simulation is executed at each integration point of the macroscale problem. Every microscale problem is solved by downscaling the macroscale values of the corresponding macroscale point (vector $\mathbf{X}$ defined in Eq. (2)) and applying boundary conditions according to the procedure described in Sec S5.

The constitutive equations of the macroscale problem are not a priori-defined and are replaced by numerically obtained constitutive relations. Upon solving the microscopic boundary value problem, the macroscopic quantities $\mathbf{q}_\mathrm{M}$ and $\mathbf{i}_\mathrm{M}$ and the macroscopic constitutive tangents $\mathbf{K}_\mathrm{q}$ and $\mathbf{K}_\mathrm{i}$ are determined from the microstructural analysis through Eqs. (14) and (15), respectively. From the numerical implementation perspective, the counterparts of Eqs. (14) and (15) are Eqs. (S.31) and (S.38), respectively.

Once the constitutive relations are known, the macroscale problem is solved through standard FE procedures. The solution of the non-linear problem is determined through a Newton–Raphson iterative procedure, making it necessary to define the macroscale constitutive tangents (15). The values stored in the $\mathbf{X}$ vectors corresponding to each macroscopic integration point are updated to move the macroscopic computation further. This set of operations is repeated for each time step of the macroscale simulation. An introduction about computational homogenization procedure can be found, for example, in Ref. [40]. Details about the numerical implementation of the FE^2 framework are given in Secs S4 and S5 in the SM.

Table 1
Field variables and their physical meaning.

Approach	symbol	physical meaning
DFN	ϕ_h	homogenized electric potential
	c_h	homogenized concentration
FE^2	ϕ_M	electric potential at the macroscale
	c_M	concentration at the macroscale
	ϕ_m	electric potential at the microscale
	c_m	concentration at the microscale
single-scale	ϕ_e	electric potential at the pore-scale
	c_e	concentration at the pore-scale

3. Results and discussion

The FE^2 framework does not require an explicit definition of effective transport properties since the constitutive equation are numerically obtained from the analysis at the RVE level (Sec 2.1). As the FE^2 naturally takes into account the effect of the microstructure on the macroscopic response, in Sec 3.1 we show how information about the microstructure is embedded in the scale transition scheme. Multiscale simulations for separators made of nanoporous materials [41] are discussed in Sec 3.2, where FE^2 simulation results are verified against results obtained from a single-scale simulation. Exploiting the findings of the first application, a simplified alternative strategy to the concurrent computation of a microstructured separator is illustrated in Sec 3.3. Finally, Sec 3.4 focuses on the application of the FE^2 framework in the study of time-evolving microstructures. Table 1 lists the notation used for the field variables in the DFN model and the FE^2 framework.

We remark that bulk properties are isotropic (scalar terms) in all the examples considered, and thus the macroscopic anisotropy exclusively results from the microstructure geometry.

3.1. Effective transport properties

In this section we show that a generalization of the effective properties used in the DFN model [1] is embedded in the tangent matrices $\mathbf{K}_\mathrm{q}$ and $\mathbf{K}_\mathrm{i}$ (Eq. (15)). For completeness we recall the basic concepts of the DFN model.

For battery cell separators, a DFN model is obtained by replacing the bulk diffusivity D_e and conductivity κ_e with their effective counterparts (D_eff and κ_eff, respectively) in Eq. (4) and inserting the so-obtained constitutive equations into Eq. (1). Since the DFN model describes the separator as an homogenized continuum, the homogenized variables c_h and ϕ_h replace c_M, c_m, and ϕ_m in all the equations leading to

$$\epsilon\frac{\partial c_\mathrm{h}}{\partial t} + \nabla\cdot\left(-D_\mathrm{eff}\,\nabla c_\mathrm{h}\right) = 0, \tag{16a}$$

$$\nabla\cdot\left(-\kappa_\mathrm{eff}\,\nabla\phi_\mathrm{h} + \kappa_\mathrm{D,eff}\,\nabla\ln c_\mathrm{h}\right) = 0. \tag{16b}$$

Equatio (16a) is obtained by substituting Eq. (4a) into Eq. (1a), taking into account that the current density is divergence free (Eq. (1b)), and considering a constant transference number t_e. The effective diffusivity D_eff and ionic conductivity κ_eff are determined adjusting bulk properties D_e and κ_e through the coefficient δ that accounts for the effect of the microstructural geometry (e.g., transport-blocking phases that are part of porous battery cell components) on the macroscopic transport response. The effective transport coefficient δ is implicitly defined through the relations

$$D_\mathrm{eff} = D_\mathrm{e}\,\delta, \quad \kappa_\mathrm{eff} = \kappa_\mathrm{e}\,\delta. \tag{17}$$

The effective diffusional conductivity $\kappa_{D,\text{eff}}$ is defined by means of Eq. (4c) by replacing κ_e with κ_{eff}.

Note that the notion of an effective transport coefficient is in principle valid only when D_e and κ_e are constant. Since the geometrical features of the microstructure are often described in terms of porosity ϵ and tortuosity τ (that 'quantifies the resistance to diffusion caused by the convolution of the pore network' [4]), the effective transport coefficient is described through the relation [4,41,42]

$$\delta = \frac{\epsilon}{\tau}, \tag{18a}$$

usually expressed as

$$\delta = \epsilon^{\alpha}. \tag{18b}$$

The last expression is obtained by describing the correlation between porosity and tortuosity through an exponential law (an approach attributed to Bruggeman [5,43]).

Three major concerns emerge with the procedure just described ((16)–(18)). First, the homogenization strategy implicitly used in the DFN model implies that the effective properties (D_{eff} and κ_{eff}) can only be related to the homogenized concentration c_h when concentration-dependent bulk properties need to be accounted for [44]. Indeed, any information about the pore-scale concentration c_e is lost when using the DFN model. The question then arises as to how well relation (17) with $D_e(c_h)$ and $\kappa_e(c_h)$ approximates the actual dependence of the effective properties on the homogenized concentration c_h. Second, even if in most applications of interest the relationship $\tau = \epsilon^{1-\alpha}$ describes the dependence of tortuosity on porosity to a good approximation [5], the value of coefficient α is problem-specific. Microstructures with identical porosity yield different exponents, and thus different transport properties, depending on their actual morphology and transport direction. Numerical simulations performed on microscopic volume elements (either numerically generated or reconstructed from real battery microstructures) have been used to determine either tortuosity τ [4,9–12,45,46], exponent α [8], or the effective transport properties (17) [3,7,8] for porous battery cell components with arbitrary microstructures. The reader can refer to Tjaden et al. [5] for a recent review on tortuosity evaluation strategies in electrochemical devices. Furthermore, since battery cell components undergo deformation during charge/discharge processes, effective properties should be updated according to the morphology evolution throughout the process. Third, δ should account for cross-terms in a multidimensional framework. In the numerical frameworks used for instance in Refs. [3,4,10,45] for determining the effective transport coefficient δ, the authors applied boundary conditions to a pair of opposite boundaries and insulated the others. These boundary conditions enable the determination of transport property in one specific direction implicitly assuming the absence of cross-terms, a treatment adequate for isotropic media only (whose effective transport properties can be characterized by a scalar δ). Although a tensorial description [13–16] appears appropriate, the description of transport properties through a vector that defines the tortuosity along three arbitrarily selected orthogonal directions is a widespread practice in the characterization of electrochemical devices [5]. A notable exception is represented by the contribution by Ebner and Wood [47], even if they do not discuss the relevance of cross-terms on the performance prediction of battery cell components. For media with arbitrary microstructures (resulting in anisotropic macroscopic responses), cross-terms vanish only if effective properties are evaluated along the principal directions, which is not necessarily the case for through-plane (main direction of transport between the electrodes) and in-plane directions in porous battery components. It follows that, in general, the evaluation of effective properties along the through-plane direction and two in-plane directions [4,9–12] does not provide a comprehensive evaluation of the transport properties.

We now show that the three concerns just described are properly addressed through our FE^2 approach. The consistent tangents $\mathbf{K}_q$ and $\mathbf{K}_i$ (Eq. (15)) incorporate the most general dependence of mass flux $\mathbf{q}_M$ and current density $\mathbf{i}_M$ on concentration, potential, and their gradients. Nonlinear microscale constitutive relations are thus transferred from the micro- to macro-scale avoiding the inconsistencies related to the use of simplified effective transport properties in Eq. (17). To prove this, we show that our homogenization approach naturally accounts for the dependence of the macroscopic response on i) concentration-dependent bulk properties (Sec 3.1.1), and ii) the contribution of the geometrical features of the microstructure. The tensorial nature of the relationship between macroscopic fluxes $\mathbf{q}_M$ and $\mathbf{i}_M$ and driving forces ∇c_M and $\nabla \phi_M$ is discussed in Sec 3.1.2. To this end, we determine $\mathbf{K}_q$ through the numerical procedure described in Sec S4.3 in the SM and we analyze the components that express the relationships between $\mathbf{q}_M$ and ∇c_M (recall the definitions of $\mathbf{K}_q$ in Eq. (15), and $\mathbf{X}$ in Eq. (2)). We thus define the macroscale diffusivity tensor [16] as

$$\mathbf{D}_{\text{eff}} = \begin{bmatrix} D_{11} & D_{12} \\ D_{21} & D_{22} \end{bmatrix}, \tag{19}$$

where D_{ij} with $i, j = 1, 2$ are the components of $\mathbf{K}_q$ according to Eq. (S39a). Moreover, we name the tensor

$$\boldsymbol{\delta} = \frac{\mathbf{D}_{\text{eff}}}{D_e} = \begin{bmatrix} \delta_{11} & \delta_{12} \\ \delta_{21} & \delta_{22} \end{bmatrix}, \tag{20}$$

which contains the effective transport coefficients δ_{ij}, the 'tensor of effective transport coefficients'. We stress that since diagonal D_{ii} and off-diagonal D_{ij} (with $i \neq j$) components are, in general, nonzero, the same holds for the components of tensor $\boldsymbol{\delta}$. Off-diagonal terms D_{ij} (δ_{ij}) with $i \neq j$ are simply the cross-terms previously mentioned; these terms are also referred to as rotatory diffusivity coefficients [16]. The same procedure applied to $\mathbf{i}_M$ and $\nabla \phi_M$ leads a tensor of effective transport coefficients $\boldsymbol{\delta}$ that is numerically identical to Eq. (20). In passing, it is worth stressing that the off-diagonal terms of the diffusivity tensor are a typical example of structure-material property relationship. They have to be considered as the numerical objective evidence of an anisotropic response stemming from an underlying non-homogeneous microscopic structure, a non homogeneous distribution of material properties, or a combination or both.

The results shown in Secs 3.1.1 and 3.1.2 were obtained with simulations performed at the microscale level, where the microscale boundary conditions for the determination of the effective transport properties are defined by the downscaled macroscale quantities

$$\mathbf{X} = \left[11.2 \times 10^6 \text{mol/m}^4 \quad 0 \quad c_M \quad 600\text{mV/m} \quad 0 \quad 1\text{mV}\right]^T. \tag{21}$$

Concentration and potential gradients are two-components vectors because of the two-dimensional setting. In Sec 3.1.1 we evaluate the dependence of the macroscale properties on the macroscopic concentration for c_M in the range $[0 - 3000]\text{mol/m}^3$, while the simulations reported in Sec 3.1.2 are performed setting $c_M = 1000\,\text{mol/m}^3$. As we will show, the results discussed in Secs 3.1.1 and 3.1.2 are independent of the selection of the values in $\mathbf{X}$ (except for c_M in Sec 3.1.1). For completeness, the values used in the numerical simulations are listed in (21).

A first verification about the properties extracted from tangents $\mathbf{K}_q$ and $\mathbf{K}_i$ is provided in Sec S6 in the SM, where the numerically obtained $\delta - \epsilon$ relationship for an isotropic medium

Table 2
Modeling parameters. Note that concentration c_e is expressed in mol/L.

Parameter	symbol	value	unit	ref.
diffusivity	D_e	$5.34 \times 10^{-10}\, e^{-0.65 c_e}$	m^2/s	[3]
ionic conductivity	κ_e	$0.0911 + 1.9101 c_e - 1.052 c_e^2 + 0.1554 c_e^3$	S/m	[3]
transference number	t_e	0.4		[52]
thermodynamic factor	$1 + \frac{\partial \ln f_e}{\partial \ln c_e}$	1		[1]
Faraday constant	F	96485	C/mol	
gas constant	R	8.31	J/(K mol)	
absolute temperature	T	298.15	K	

is compared against 'Bruggeman approach'. With 'Bruggeman approach' we identify an approximation of the effective properties of porous electrodes obtained calculating δ from Eq. (18b) with $\alpha = 1.5$ (determined by Bruggeman [43] for spherical non-overlapping transport obstructing phases). The evaluation of transport effective properties of porous battery components through Bruggeman approach was already in use at time of the seminal modeling work of Doyle et al. [1], and it still is a popular simple-to-compute first approximation (see, for example, Refs. [48–51]). Even if many strategies for the estimation of effective properties are available in the literature [5], the popularity of Bruggeman approach is such that it enables a straightforward comparison. For this reason the results obtained with Bruggeman approach are presented along with the results of the proposed approach.

All the results involving a RVE have been obtained considering RVEs with 16 ion-transport blocking inclusions, corresponding to a RVE size that ensures converged transport properties (refer to the study in Sec S7 in the SM for the case of elliptical inclusions).

3.1.1. Concentration-dependent transport properties

This section attempts to answer the previously raised question of how accurately Eq. (17) represents the dependence of the effective diffusivity D_{eff} and ionic conductivity κ_{eff} on the homogenized concentration c_h. We consider a liquid electrolyte consisting of $LiPF_6$ dissolved in EC-DMC (a mixture of ethylene carbonate and dimethyl carbonate). Bulk transport properties, listed in Table 2, are chosen according to Refs. [1,3,52]. In the microscale FE computation, we calculate the effective transport properties at varying macroscale concentration values c_M. The chosen RVE includes 16 randomly distributed circular inclusions (that represent the ion-transport blocking phase). Based on the $\delta - \epsilon$ relationship obtained through our numerical study on microstructures with circular inclusions (Sec S6), a coefficient $\delta = 0.31$ applies to x and y directions when $\epsilon = 0.5$. It is remarked that $\delta = 0.31$ is calculated using constant diffusivity and ionic conductivity and, therefore, it results from the microstructure.

Figure 2 shows the effective transport properties as a function of the macroscale concentration (i.e., c_h in the DFN model and c_M in the proposed FE^2 approach). The effective transport properties D_{eff} and κ_{eff}, denoted by dashed lines, are calculated via Bruggeman approach and with bulk transport properties described as a function of concentration in Table 2. This implies that the concentration dependence does not change from microscale to macroscale and a scaling factor is sufficient to reflect the microstructure geometry effect. The solid lines represent the effective transport properties (Eq. (17)) that are equal to the bulk properties multiplied by the effective transport coefficient $\delta = 0.31$ (Fig. S2). The simulated effective transport properties denoted by circles are the component D_{11} in Eq. (S39a) and κ_{14} in Eq. (S39b) at discrete macroscale concentrations c_M. Note that these effective properties are normalized by the bulk properties at concentration $c_e = 1.0$mol/L and denoted as D_{ref} and κ_{ref}.

The microscale FE simulation results overlap with those obtained with concentration-dependent bulk properties multiplied

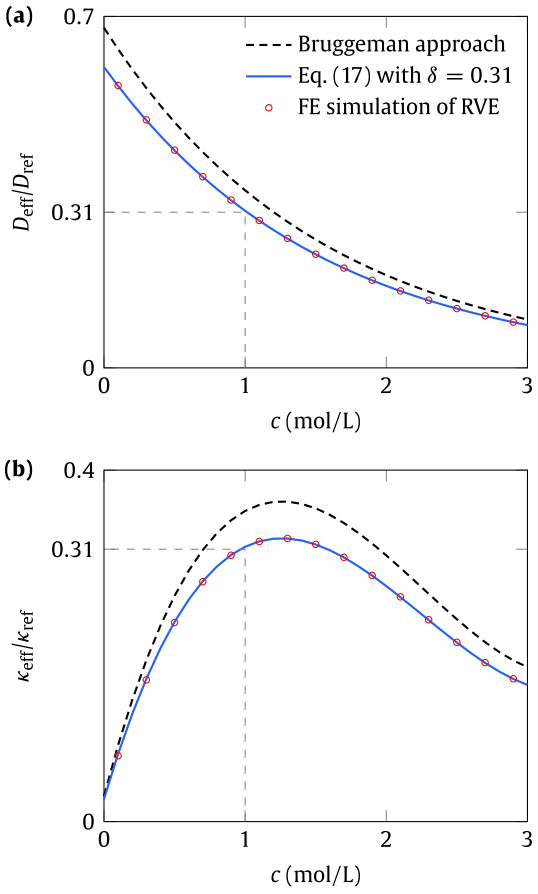

Fig. 2. Effective diffusivity D_{eff} (a) and ionic conductivity κ_{eff} (b) normalized by the bulk values at $c_e = 1.0$mol/L (i.e., D_{ref} and κ_{ref}, respectively) versus the macroscale concentration c (c_h in the DFN model combined with Bruggeman approach or c_M in the FE^2). The dashed lines are calculated via Bruggeman approach, the solid lines represent the bulk properties multiplied by 0.31 (Fig. S2 in the SM), while circles are D_{11} and κ_{14} in Eq. (S.39) at each macroscale input c_M. The RVE porosity $\epsilon = 0.5$. The bulk properties can be found in Table 2.

by the effective transport coefficient $\delta = 0.31$. This agreement addresses the first concern and verifies the incorporation of microstructure effect by directly scaling the concentration-dependent bulk properties by a microstructure-related factor (Eq. (17)). It is remarked that this observation is consistent with the volume-averaging analysis by Quintard et al. [53], and a similar relation to Eq. (17) can be reproduced based on Eqs. (24), (25), (98), and (102) in their paper. According to Quintard et al. [53], the functional relation at the macroscale can safely use the microscale one provided a length scale constraint (Eq. (26) in Quintard et al. [53]): $l_{\text{rve}} \ll l_{\text{vv}}$, where l_{rve} represents the RVE length scale and l_{vv} is the macroscale distance over which significant variations of volume-averaged field variables occur. This scale constraint will naturally

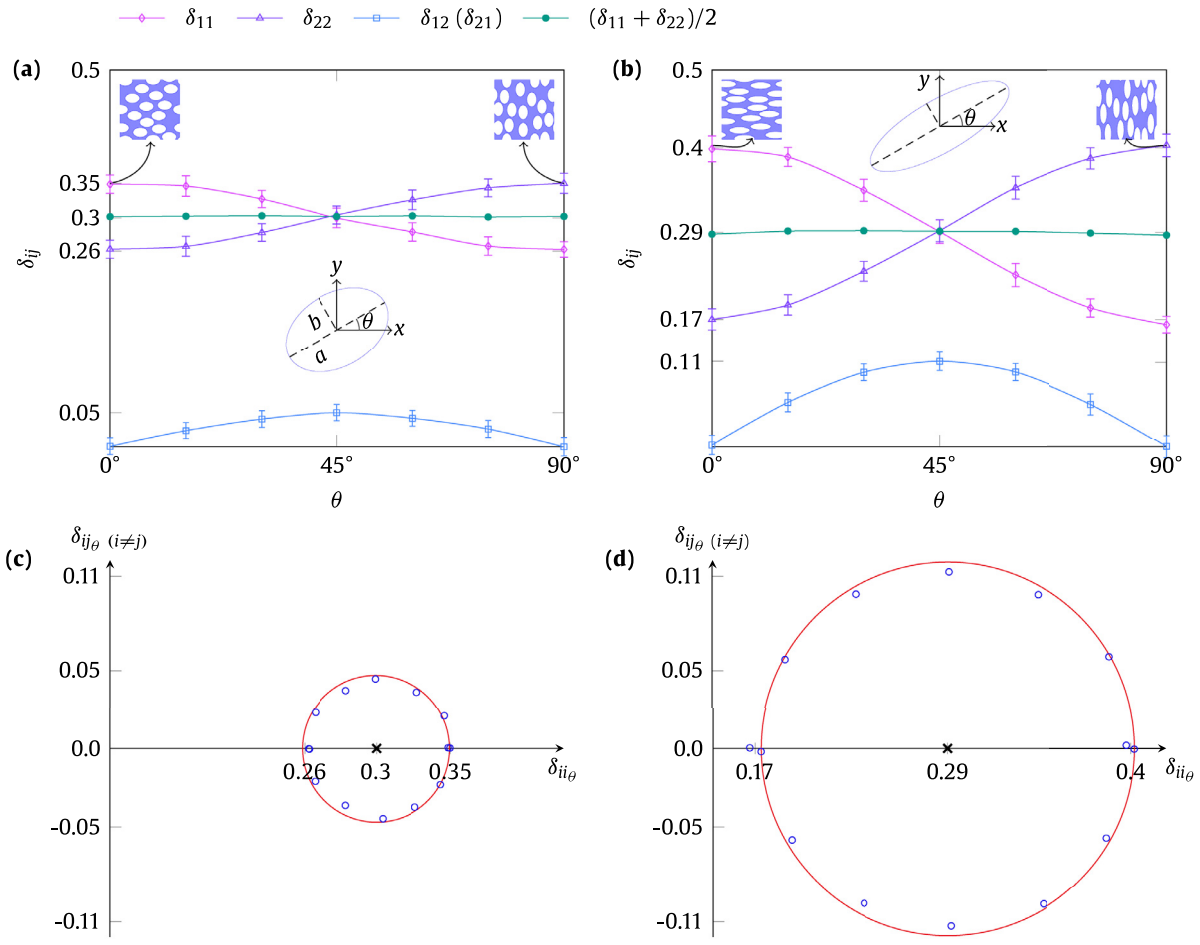

Fig. 3. Effective transport coefficients δ_{ij} in Eq. (20) versus the orientation θ of the ellipses at aspect ratio $a/b = 1.5$ (a) and 3.0 (b). The subscripts 1 and 2 are associated with the x and y directions, respectively. The diagonal components δ_{11} and δ_{22} are the transport coefficients in the x and y directions, respectively, while the off-diagonal components δ_{12} and δ_{21} reflect the influence of concentration gradient in the y direction on the mass flux in the x direction and vice versa. In the simulation the bulk properties (D_e and κ_e) are isotropic and constant. The porosity is held constant at 0.5 (i.e., the total area of the ellipses is fixed). Panels (c) and (d) show the Mohr's circles in the $\delta_{ii_\theta} - \delta_{ij_\theta\ (i\neq j)}$ coordinate system related to the results in panels (a) and (b). Subscript θ indicates that coefficients $\delta_{ij\ (i,j=1,2)}$ relate to the microstructure inclination θ.

be satisfied when the principle of scale separation [32,37] of the FE^2 method holds.

3.1.2. Anisotropic effective transport properties

The morphology of the ion-transport blocking phase (e.g., separator membranes [54]) is crucial for the overall ionic transport process taking place in battery cell separators as the microstructure of the porous separator determines the macroscopic response of the system. In this section we aim to investigate the capability of our multiscale framework to capture this dependence, especially for microstructures that determine an anisotropic macroscopic response.

The study is performed by generating microstructures with porosity $\epsilon = 0.5$ characterized by different morphologies, and analyzing the components of $\boldsymbol{\delta}$ in Eq. (20). We consider RVEs filled with randomly distributed elliptical inclusions (representing the ion-transport blocking phase) surrounded by the electrolyte. In these RVEs, the position of an ellipse is random but its orientation θ is fixed, ranging from 0 to 90°. For each orientation we generate 100 RVE configurations taking isotropic and constant (i.e., not concentration-dependent) microscale bulk properties D_e and κ_e. Two families of morphologies are generated considering transport-blocking ellipses, characterized by semi-major axis a and semi-minor axis b, with aspect ratio a/b values equal to 1.5 and 3. Each point in Fig. 3 represents the average of 100 RVE (the standard deviations is also shown).

Figure 3 a shows that the diagonal component δ_{11} in the x direction is maximized at $\theta = 0$, that is, when the major axis of the ellipse is aligned along the x direction. As the major axis is progressively aligned with the y direction (θ increases), δ_{11} keeps decreasing and reaches the minimum at $\theta = 90°$. The effective transport coefficient δ_{22} in the y direction show an opposite trend with respect to δ_{11}; their behavior reverses at $\theta = 45°$ where their values coincide. These observations are consistent with the outcome of the three-dimensional investigation performed in Ref. [46]. Yan et al. [46] show that the alignment of ellipsoidal particles along a certain direction results in a lower tortuosity along the direction of alignment compared to directions orthogonal to it (recall the inverse proportionality (18) that relates tortuosity τ and effective transport coefficient δ). The values of the off-diagonal components δ_{12} and δ_{21} coincide, in agreement with theoretical predictions for (uncoupled) diffusion phenomena in anisotropic media [16], reach a maximum at $\theta = 45°$, and show a symmetry with respect to $\theta = 45°$.

In the simulations, we fix the coordinate system and rotate the angle of alignment of the elliptical phase for the sake of compu-

tational convenience. The outcome is analogous to a rotation of the coordinate system. This observation and the results reported in Fig. 3a allow us to draw a parallel with solid mechanics in the sense that the numerically evaluated $\boldsymbol{\delta}$ can be understood as a tensor, i.e., an object that is used to describe physical properties and obeys certain transformation rules. More specifically, the connection of $\boldsymbol{\delta}$ to physical properties is rooted in its definition (the effective transport coefficients δ_{ij} are extracted from $\mathbf{K}_\mathrm{q}$ (Eq. (S39a)) according to Eqs. (19) and (20)). Whether or not $\boldsymbol{\delta}$ can be considered representative of the actual effective transport properties associated to a given microstructure can be ascertained by means of an analysis of the results reported in Fig. 3a. The results indicate that these properties do not change with rotations of the coordinate system as demonstrated by the invariance of the mean value of δ_{11} and δ_{22} (0.30 and 0.29 for $a/b = 1.5$ and 3.0, respectively) with respect to θ. It can also be shown that the spectrum of $\boldsymbol{\delta}$ is invariant, implying that $\boldsymbol{\delta}$ is indeed a sound representation of the effective transport coefficients for a given microstructure. The definition of $\boldsymbol{\delta}$ as 'tensor of effective transport coefficients' is therefore justified.

In solid mechanics, Mohr's circle is a two-dimensional graphical representation of the state of stress at a point. Since the transformation of δ_{11}, δ_{22}, and δ_{12} with θ should be consistent (at least in theory [16]) with the coordinate transformation of tensor components, Mohr's circle [55] can be used to represent transport coefficients in multidirectional transport processes, an approach recently taken in Yang and Qin [56]. Figure 3b shows the Mohr's circles for the data represented in Fig. 3a. For convenience, the analytical expressions of the circles is defined with reference to the microstructures oriented at $\theta = 0$ or 90°. At these orientations, the off-diagonal terms $\delta_{12} = \delta_{21} = 0$ and the direct terms δ_{11} and δ_{22} are used to define center (as their mean value) and diameter (as their difference). As a confirmation of the validity of the coordinate transformation rules of tensor components, the application of Mohr's transformation rules to each data point in Fig. 3a results in the placement of these points on the circles. In analogy with the use of Mohr's circle in stress analysis, as soon as the effective transport coefficients at a point are known, it is therefore immediate to identify the principal directions (i.e., the directions such that the off-diagonal terms δ_{ij} are zero) and the effective transport coefficients acting on a plane at a generic inclination passing through that point.

We recognize that restricting the numerical simulation to a two-dimensional setting is rather simplistic and might affect the interpretation of the results and their generalization to the characterization of porous media. In fact, the description of porous structures that result in macroscopic anisotropic properties can sensibly vary if a three-dimensional investigation is performed in place of a two-dimensional one (refer, for example, to Yan et al. [57]). Nevertheless, in spite of the simplified representation of the microstructure, our numerical results are consistent with Ebner et al.'s [10] experimental observations about the effect of particle shape and orientation on the tortuosity of three-dimensional battery electrode microstructure. Ebner et al. [10] report values of tortuosity τ (Eq. (18a)) around 1.46 for NMC electrodes consisting of spherical active particles. By converting the values of δ obtained through our numerical simulations into τ, we obtain a tortuosity equal to 1.61 for a RVE filled with random circular inclusions (Fig. S2). Ebner et al. [10] observe that, if elongated particles make up the electrodes, the particles tend to align with their longest axis parallel to the current collector (perpendicular to the direction of flow). We thus focus on the values that pertain to the x direction at $\theta = 90^\circ$ (Fig. 3) for the comparison. Ebner et al. [10] report through-plane tortuosities for LCO (ellipsoide-like particles) and graphite (platelets-like particles) electrodes equal to 1.77 and 3.76, respectively. The increase of tortuosity for increased particles aspect ratio is in good agreement with our results: taking the value of δ_{11} at $\theta = 90^\circ$, we observe that the tortuosity increases from 1.9 to 2.9 as the aspect ratio increases from 1.5 to 3 (Fig. 3), respectively. The qualitative agreement in terms of tortuosity change validates the proposed numerical approach.

The Mohr's circle representation captures the degree of anisotropy: the more pronounced the anisotropy (the higher the aspect ratio a/b), the bigger the radius of Mohr's circle (in the limit case of isotropic response, the circle collapses to a point). Two conclusions follow. First, the measure of anisotropy proposed by Cooper et al. [4], based on the difference between the maximum and minimum transport properties along arbitrary orthogonal directions, may not provide a comprehensive representation of anisotropy. The anisotropy degree can be evaluated as the difference between the maximum and minimum principal transport properties along the principal directions only (i.e., when off-diagonal components are null) [56]. Second, since the transport direction between electrodes is in general not the principal, the off-diagonal components of the effective diffusivity tensor should not be disregarded a priori. In Appendix A the metric proposed by Cooper et al. [4] and Mohr's radius are used to evaluate the degree of anisotropy of a selection of porous battery materials.

3.2. Comparison with single-scale simulation results and DFN model prediction

In this section we employ the multiscale approach to characterize ionic transport in a battery cell separator with a microstructure that yields an anisotropic macroscopic response. As a verification of the FE^2 framework, the multiscale simulation results are compared with those obtained from a single-scale simulation in which the separator microstructure is fully resolved. The single-scale simulation is performed by substituting Eq. (4) into balance equations

$$\frac{\partial c_\mathrm{e}}{\partial t} + \boldsymbol{\nabla} \cdot \mathbf{q}_\mathrm{e} = 0 \quad \text{and} \tag{22a}$$

$$\boldsymbol{\nabla} \cdot \mathbf{i}_\mathrm{e} = 0 \quad \text{in} \quad V_\mathrm{e} \times (0, t_\mathrm{end}). \tag{22b}$$

In such case, $c_\mathrm{e} = c_\mathrm{m}$, $\mathbf{q}_\mathrm{e} = \mathbf{q}_\mathrm{m}$, and $\mathbf{i}_\mathrm{e} = \mathbf{i}_\mathrm{m}$. Notice that neither homogenization strategies nor effective properties are used with this approach. This example shows the ability of the FE^2 method to properly account for all terms of the effective transport property tensor and highlights the relevance of the off-diagonal terms for a proper evaluation of the macroscopic response. The prediction capabilities of the DFN model, which uses scalar effective transport properties, are also discussed.

We simulate a porous separator consisting of a regular array of unit cells. Each unit cell contains an elliptical ion-transport blocking phase surrounded by the electrolyte as shown in Fig. 4a. Figure 4b shows the discretization of the multiscale problem domains at both scales. At each integration point of the macroscale mesh, we attach the microscale RVE, which is equal to a unit cell. For the single-scale simulation, we consider 100×40 unit cells as shown in Fig. 4c. Numerical studies (not reported here) confirm that the results obtained with each approach can be considered converged. Here we use the concentration-dependent transport properties listed in Table 2.

The RVE of choice is not representative of the morphology of a real separator; as such, the numerical results are not meant to replicate the response of a real battery separator. The RVE shown in Fig. 4 has been selected for numerical convenience only and it is functional to our purpose (verification of the FE^2 framework). The steady state assumption for the microscale formulation (3) is discussed in Sec S8 in the SM with reference to the geometrical setting considered here.

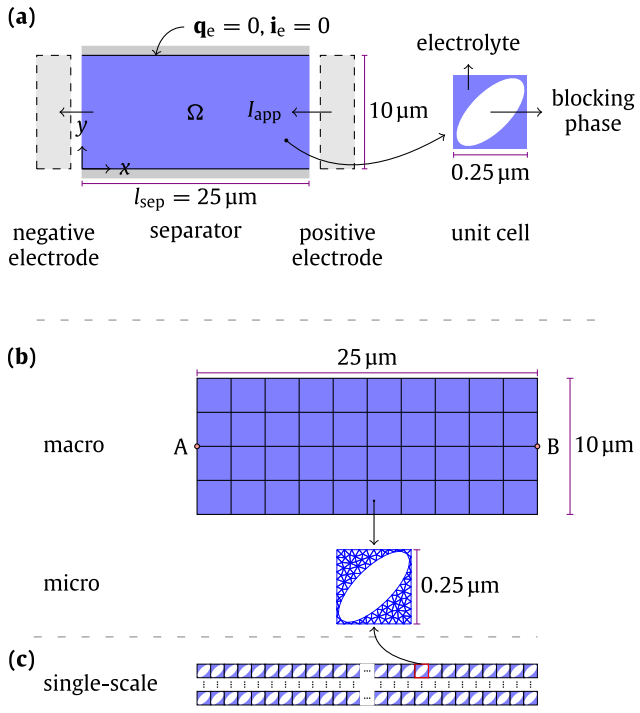

Fig. 4. Panel (a) illustrates the problem setting. The RVE porosity is 0.5, and the electrolyte properties are listed in Table 2. Panel (b) shows the computational mesh for the FE^2 method: 10×4 four-node quadrilateral elements are used for the macroscale mesh and 204 three-node triangular elements for the RVE mesh. The single-scale discretization in panel (c) consists of 100×40 unit cells, with each unit cell discretized as the RVE.

In accordance with the galvanostatic charge process, a constant current density I_{app} and a constant lithium ion mass flux are enforced. In addition, the electric potential at the leftmost boundary ($x = 0$) is set to zero as the reference value. Boundary and initial conditions are expressed as

$$\mathbf{i}_M \cdot \mathbf{n}|_{x=l_{sep}} = -I_{app}, \quad \phi_M|_{x=0} = 0, \tag{23a}$$

$$\mathbf{q}_M \cdot \mathbf{n}|_{x=l_{sep}} = -\frac{I_{app}}{F}, \quad \mathbf{q}_M \cdot \mathbf{n}|_{x=0} = \frac{I_{app}}{F} \quad \text{for } t \in (0, t_{end}), \tag{23b}$$

and

$$c_M = c_0 \quad \text{at } t = 0 \text{ in } \Omega, \tag{23c}$$

respectively. We apply a current density $I_{app} = 300\text{A/m}^2$, equivalent to a 10 C charge rate for commercial graphite-NMC battery cells [9,58]. The initial concentration c_0 in the whole separator domain Ω is specified at 1000mol/m^3. The simulation ends at $t_{end} = 4$s when steady-state is achieved. The above boundary and initial conditions for the multiscale problem also hold for the single-scale approach.

The results are reported in Fig. 5. Panels (a) and (c) show the steady-state ionic concentration and electric potential distribution, respectively, along three horizontal lines (bottom: $y = 0$, middle: $y = 5\mu$m, and top: $y = 10\mu$m), while panels (b) and (d) show the concentration and potential profiles, respectively, along three vertical lines (leftmost: $x = 0$, middle: $y = 12.5\mu$m, and rightmost: $y = 25\mu$m). The circles represent the macroscale solution c_M and ϕ_M from the FE^2 method; the solid lines denote the single-scale simulation results, i.e., the intrinsic volume averages $\langle c \rangle_e$ and $\langle \phi \rangle_e$. Initially, the concentration is uniform in the x and y directions; as the current flows, a concentration gradient starts to develop, resulting in a concentration decrease at the leftmost edge and a concentration increase at the rightmost boundary. Since the off-diagonal terms of the tensor of effective transport coefficients (20) are not null (refer to (24)), both components (in x and y directions) of the macroscopic flux q_M are affected by both components of the macroscopic gradients. It follows that, despite the insulated top and bottom boundaries, field variable gradients develop in the y direction to counterbalance the contribution by the off-diagonal terms (δ_{12} and δ_{21} in Fig. 3). A discussion about this effect is provided in Sec S9 in the SM.

Besides the steady-state profiles, we show the concentration evolution at the middle points of the vertical edges in panel (e). Panel (f) reports the temporal evolution of the potential drop from point B to A and provides an indication of the ohmic loss attributable to the separator. The figure shows that the multiscale simulation results adequately match the single-scale simulation results, verifying the multiscale framework (and the scale transitions described in Secs 2.3 and 2.4). In this example, we specifically choose the inclination $\theta = 45^\circ$ for the inclusion in order to maximize the off-diagonal values (according to Fig. 3), causing evident concentration and potential gradients in the y direction. The variation in the y direction is obviously not seen in the results pertaining to the DFN model combined with Bruggeman approach (dashed lines in all the panels).

For the morphology at hand, the evaluation of the tensor of effective transport coefficients by means of the proposed approach leads to

$$\boldsymbol{\delta} = \begin{bmatrix} 0.31 & 0.13 \\ 0.13 & 0.31 \end{bmatrix}. \tag{24}$$

Two remarks are needed at this stage. First, the values reported in (24) are comparable with those shown in Fig. 3b, where $\delta_{11} = \delta_{22} = 0.29$ and $\delta_{12} = \delta_{21} = 0.11$ at $\theta = 45^\circ$ (the relative difference is approximately 7% and 15% for diagonal and off-diagonal terms, respectively). We stress that the geometry of the transport-blocking phase considered in this section is similar to that of Sec 3.1.2 (aspect ratio of the ellipse is $a/b = 2.5$ and $a/b = 3.0$, respectively), while the spatial distribution of the transport-blocking phase is remarkably different (the arrangement is regular in this section, and random in Sec 3.1.2). The effect of orientation and shape (of transport-blocking inclusions) on the tensor of effective transport coefficients is dominant with respect to the effect of the spatial arrangement (recall that porosity is unchanged, $\epsilon = 0.5$ in both investigations). This observation is consistent with the conclusion of Ebner et al. [10,47]. Second, if the off-diagonal terms of (24) are dropped, the tensor of effective transport coefficients reduces to $\boldsymbol{\delta} = 0.31\mathbf{I}$. Bruggeman approach with $\epsilon = 0.5$ leads to $\delta \approx 0.31$ (refer, to Fig. S2), i.e., $\boldsymbol{\delta} \approx 0.31\mathbf{I}$ (a scalar δ is equivalent to a transport property tensor with equal diagonal terms $\delta_{11} = \delta_{22} = 0.31$ and $\delta_{12} = \delta_{21} = 0$). This means that (for the morphology at hand) any approach incapable of taking the off-diagonal terms into account leads to a response prediction that is equivalent to that of Bruggeman approach, and it is thus characterized by the same level of (in)accuracy. In this regard, panels (b) and (d) in Fig. 5 show the differences in the concentration and potential field prediction caused by the absence of off-diagonal terms; the 27% discrepancy in the prediction of the potential drop across the separator with respect to single-scale and FE^2 approaches shown in panel (f) is noteworthy.

An estimate of the extent of the off-diagonal terms in real porous battery material is provided for reference in Appendix A (Table A.1).

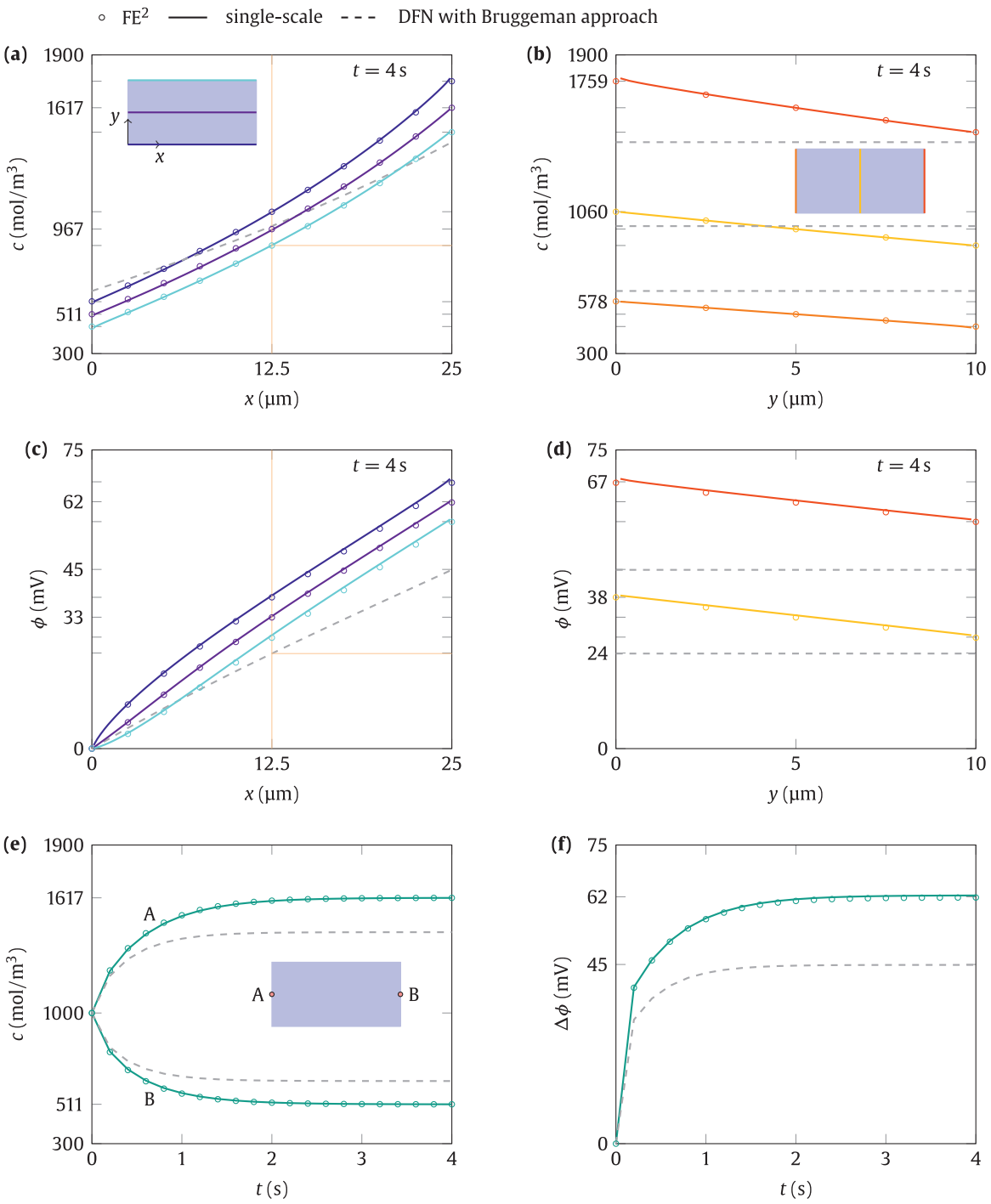

Fig. 5. Comparison between FE^2 calculation and single-scale simulations. Panels (a) and (c) show concentration c and potential ϕ, respectively, along the x direction at $y = 0$, 5, and 10μm in the steady state ($t = 4$s); correspondingly, panels (b) and (d) show concentration c and potential ϕ along the y direction at $x = 0$, 12.5, and 25μm. Here c and ϕ refer to c_{M} and ϕ_{M} for the FE^2 method, c_{h} and ϕ_{h} for the DFN model with Bruggeman approach (Table 1), and the intrinsic volume averages $\langle c\rangle_{\mathrm{e}}$ and $\langle\phi\rangle_{\mathrm{e}}$ for the single-scale simulations. Panel (e) shows the temporal evolution of the concentration at point A and B, which are located at the center of the leftmost ($x = 0$) and rightmost ($x = 25\mu$m) boundaries of the separator, respectively. Panel (f) shows the temporal evolution of the potential drop $\Delta\phi$ from point B to A across the separator, i.e., the potential at point B with reference to a prescribed null potential at the leftmost boundary.

3.3. A simplified alternative strategy to the FE^2 method

The results described in Secs 3.1.1, 3.1.2 and 3.2 suggest that the description of the most general transport processes (concentration-dependent bulk properties and anisotropy) can be attained by defining effective transport properties as

$$\mathbf{D}_{\mathrm{eff}} = D_{\mathrm{e}}(c_{\mathrm{h}})\,\boldsymbol{\delta}, \quad \text{and} \quad \boldsymbol{\kappa}_{\mathrm{eff}} = \kappa_{\mathrm{e}}(c_{\mathrm{h}})\,\boldsymbol{\delta}, \tag{25}$$

where $D_{\mathrm{e}}(c_{\mathrm{h}})$ and $\kappa_{\mathrm{e}}(c_{\mathrm{h}})$ are concentration-dependent bulk properties, and using Eq. (25) in a DFN model. In this section, we as-

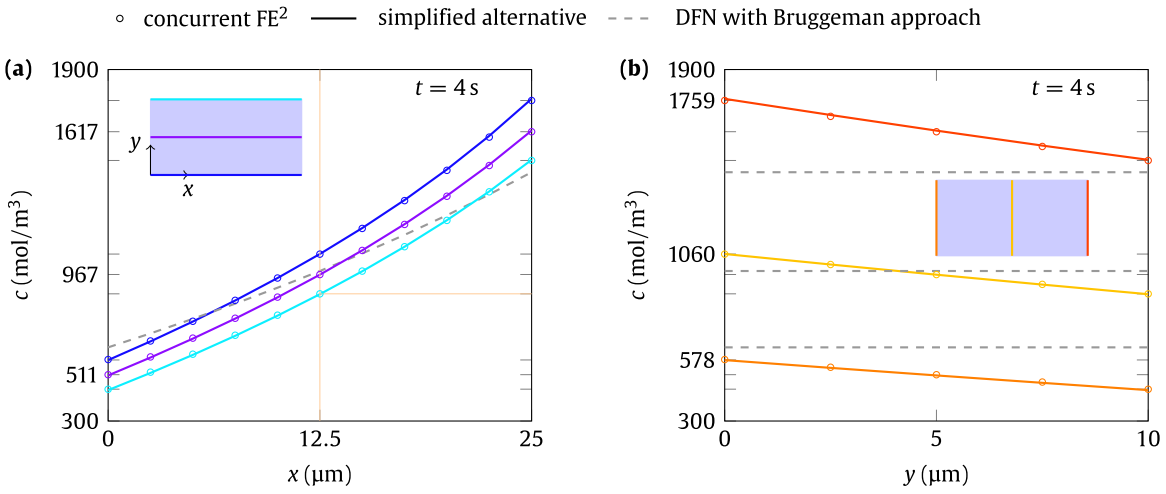

Fig. 6. Comparison of the results obtained with the simplified alternative strategy and the concurrent FE^2 approach. The problem setting is reported in Fig. 4a. The results of the concurrent FE^2 approach and the DFN model with Bruggeman approach are shown in Fig. 5a and b. The simplified alternative strategy results are obtained by solving Eq. (16) with the effective transport properties evaluated according to Eq. (25) and the tensor $\boldsymbol{\delta}$ with a single microscale simulation (RVE in Fig. 4a) according to Sec 2.4 (and the numerical implementation described in Sec S4.3 in the SM).

sess the validity of such a simplified approach by pre-computing $\boldsymbol{\delta}$ with a single microscale simulation according to Sec 2.4 (and the numerical implementation described in Sec S4.3 in the SM). To this end, we consider the problem setting of Sec 3.2.

The results obtained with the simplified approach and those of the FE^2 method, contrasted in Fig. 6, show a perfect agreement. The agreement suggests that the effective transport properties (Eq. (25) with pre-computed $\boldsymbol{\delta}$) perfectly match the numerical tangents in Eq. (15) computed through the FE^2 and confirm that the conclusions drawn in Sec 3.1.1 for the isotropic macroscopic response hold true also when the macroscopic response is anisotropic. The results of the DFN model combined with Bruggeman approach (dashed lines in Fig. 6) are reported to show the outcome of a generic approach that evaluates δ_{11} and δ_{22} without taking the off-diagonal terms into account. The (erroneous) conclusion would be that the response is isotropic because $\delta_{11} = \delta_{22}$. However, the single-scale simulation show that this is not the case. The response of the material is not isotropic because the off-diagonal terms do not vanish in the coordinate system of choice. This means that the coordinate system that results in $\delta_{11} = \delta_{22}$ is not the principal reference system. Thanks to the analogy with the results of Sec 3.1.2 we can refer to Fig. 3c and 3 d and deduce that the principal coordinate system, the one for which $\delta_{12} = \delta_{12} = 0$, is such that $\delta_{11} \neq \delta_{22}$ (either for $\theta = 0$ or 90°). The macroscopic response is actually anisotropic. The 'simplified alternative strategy' properly addresses the macroscopic description of the medium as it preserves the tensorial nature of the effective transport properties.

3.4. An example with time-evolving microstructure

The examples discussed in Secs 3.2 and 3.3 assume that the microstructure does not evolve during a (dis)charge process. However, (dis)charge processes are often accompanied with expansion/contraction of the electrodes [59], leading to dynamic microstructure changes of the separator membrane [34]. Moreover, additional deformations may be induced by external mechanical loading [6,9]. When the separator membrane deforms, a concurrent porosity ϵ and tortuosity τ change takes place [9], thus affecting the overall system response (recall relation (18a)). Lagadec et al. [9] showed that when the separator membrane is subject to a significant deformation level (up to 40%), the effective transport coefficient reduces by 96% in the through-plane direction of the separator layer, thus making the separator the limiting component of the cell operations even at a modest C-rate of 0.75 C.

As the FE^2 approach ensures that the tensorial nature of the transport properties is correctly captured, it can be employed to address the effect of an evolving microstructure. The FE^2 framework presented in this contribution allows accounting for transport properties changes through morphology changes in a consistent manner. For simplicity, we show an example where the microstructure morphology evolves at constant porosity $\epsilon = 0.5$. The macroscale problem setting is that of Sec 3.2, but the RVE contains 16 ellipses. We consider two morphology evolutions with coincident initial and final configurations, but different evolution patterns (I and II according to Fig. 7a and b). The morphology change is introduced by changing the aspect ratio a/b of the ellipses from 3 to 1/3. For each aspect ratio value, we generate 50 RVE samples and calculate the average transport properties; we then select a RVE with transport properties that are closer to the average values. The total simulation time ($t_{\text{end}} = 4$s) is about three times larger than the time required to achieve the steady state with a non-evolving microstructure (dashed line in Fig. 7). Pattern I and II are implemented by updating the RVE geometry at different stages. In pattern I the RVE is updated at regular intervals of time from $t = 0$ to $t = 4$s (Fig. 7 a). In pattern II the final configuration is attained at $t = 2$s and remains unchanged until $t = 4$s (Fig. 7 b). Since the semi-major axes of the ellipses are always aligned with the x and y directions (Fig. 7a and b), we stress that these directions are principal and hence the off-diagonal components (δ_{12} and δ_{21}) are null (Fig. 3).

The temporal evolution of the maximum/minimum concentration and potential drop across the separator are plotted in Figs. 7c and d. The dashed lines in Fig. 7 are the results of the DFN model combined with Bruggeman approach, which does not account for the microstructure evolution. Figure 7c and d show that when the microstructure evolution is disregarded, the steady-state configuration is attained after roughly 1s, while both c and $\Delta\phi$ change during the whole process when either one of pattern I and II is considered. A noticeable difference between the system response under the different morphology patterns is the energy loss. The energy dissipated during the simulated process is proportional to the

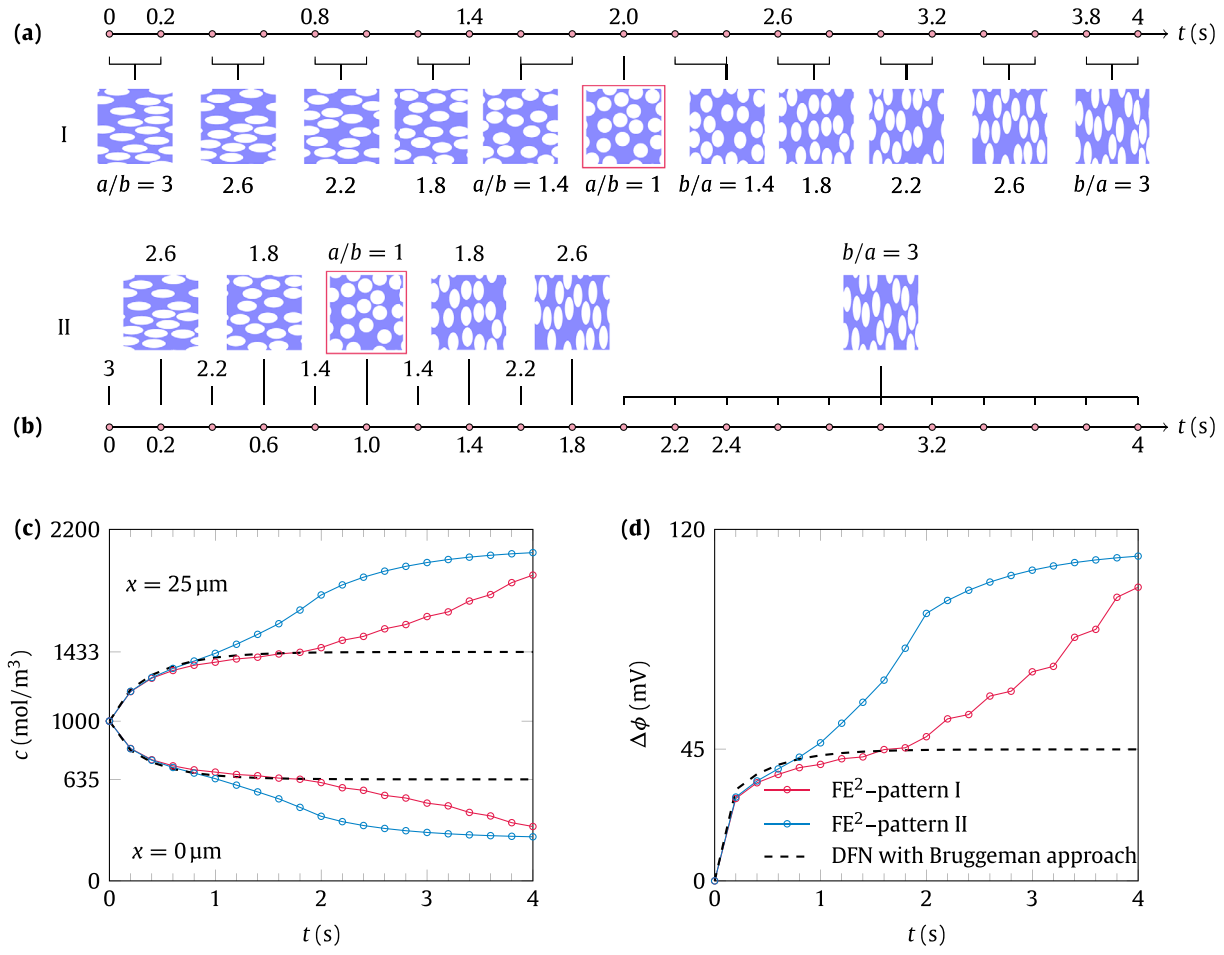

Fig. 7. FE^2 simulation of a separator with time-evolving microstructure. The 4s simulation time is discretized into 21 time steps. The microstructure evolves with time following two different patterns (I in panel (a) and II in (b)) at constant porosity equal to 0.5. Panel (c) shows the temporal evolution of the maximum and minimum concentrations computed by the FE^2 method under pattern I and II and by the DFN model that only considers porosity. Panel (d) shows the potential drop across the separator. Here c and ϕ refer to c_M and ϕ_M in the FE^2 method and c_h and ϕ_h in the DFN model, respectively.

integral of the potential drop ($\Delta\phi$, Fig. 7d) with respect to time: pattern II dissipates 58.6% more energy than pattern I.

Since we showed that a morphology change alone influences the macroscopic response, we envisage that an even stronger modification of the macroscopic responses should be expected if a porosity change takes place simultaneously. We stress that even if we considered morphology evolution histories with identical initial and final configurations, the evolution pattern itself determines a remarkably different system response. This consideration emphasizes the need to monitor the microstructure evolution (and the consequent transport property changes) at adequately close time instants. On-the-fly transport property simulations based on imaged microstructures were also encouraged by Lagadec et al. [9] for improved understanding of local effects in energy storage applications. However, they also recognized that the deformation of the separator is elastic (no residual deformation upon loading removal) under low applied loadings, rendering it a challenge to image the separator microstructure at different stages of the deformation process. Our results suggest that a multiscale electrochemical-mechanical coupled model should be used to achieve this goal. In particular, a coupled FE^2 model would enable tracking the microstructure deformation evolution and the concurrent change of the electrochemical response.

4. Conclusions

We employ a FE^2 framework for the investigation of ionic transport in porous battery cell separators during (dis)charge processes. The methodology allows us to consider bulk transport properties dependent on local fields (e.g., ionic concentration within the pores of the polymeric membrane) and to account for their impact on the system response. The approach is general and is suitable for isotropic and anisotropic media. We show that the numerical framework allows simulating transport processes accounting for a concurrent change of the separator microstructure (Sec 3.4).

Simplified strategies can be used in place of the FE^2 method when microstructure deformations are negligible, i.e., when the microstructure geometry does not change during the process. Under these conditions, the DFN model is as accurate as the FE^2 strategy provided that the effective transport properties properly account for the contribution of the microstructure. To this end, the effective properties should be computed as the product of a scalar term accounting for the dependence of bulk properties on local fields and the tensor of effective transport coefficients $\boldsymbol{\delta}$. The latter can be identified through a single simulation performed on a RVE of the microstructure, with a remarkable reduction of the computational effort compared to FE^2 simulations.

At the battery cell level, transport processes mainly take place in the through-plane direction. Despite the dominant unidirectionality our results show that in-plane transport components are, in general, not null. For this reason, we emphasize the need to account for the tensorial nature of $\boldsymbol{\delta}$ and stress that both diagonal and off-diagonal components are relevant for the description of transport processes through porous battery components. Actually, if the off-diagonal components of the tensor of effective transport coefficients $\boldsymbol{\delta}$ are arbitrarily omitted, in-plane transport components cannot be captured, thus leading to incorrect prediction of the macroscopic response (Sec 3.2).

In general, morphology evolution with cycling is common to all porous components of battery cells [34]. This means that even if the 'as-produced' battery component shows an isotropic macroscopic response, some level of anisotropy may arise with cycling. A relationship between morphology evolution and transport properties evolution is not easy to identify and a FE^2 simulation strategy can provide a useful asset (Sec 3.4).

Declaration of Competing Interest

The authors declare that they have no known competing financial interests or personal relationships that could have appeared to influence the work reported in this paper.

Credit authorship contribution statement

Mingzhao Zhuo: Conceptualization, Methodology, Software, Validation, Formal analysis, Data curation, Writing – original draft, Writing – review & editing, Visualization. **Davide Grazioli:** Formal analysis, Writing – review & editing, Visualization. **Angelo Simone:** Supervision, Project administration, Funding acquisition, Writing – review & editing, Visualization.

Acknowledgements

The research leading to these results has received funding from the European Research Council under the European Union's Seventh Framework Programme (FP7/2007–2013) / ERC Grant agreement no 617972.

Appendix A. Transport properties and degree of anisotropy

Many examples of porous battery materials with direction-dependent effective transport properties have been documented in literature. We consider a selection of the data reported in Refs. [5,9,10] and evaluate the degree of anisotropy with the metric σ_C introduced by Cooper et al. [4] and through the radius r_M of the Mohr's circle associated to tensor $\boldsymbol{\delta}$, as suggested in Sec 3.1.2. The transport properties that result from the microstructure considered in our numerical simulations are assessed with the same metrics to show that their degree of anisotropy is comparable with that of real porous battery media.

Cooper et al. [4] propose the following quantity to measure anisotropy:

$$\sigma_C = \frac{\max(\tau_i) - \min(\tau_i)}{\tau_c}, \quad \text{with} \quad i = x, y, z, \tag{A.1}$$

where τ_i represents the tortuosity evaluated along three orthogonal directions (x, y, and z) that do not necessarily coincide with the principal axes. The characteristic tortuosity τ_c is defined as

$$\tau_c = 3\left(\frac{1}{\tau_x} + \frac{1}{\tau_y} + \frac{1}{\tau_z}\right)^{-1}. \tag{A.2}$$

Based on the investigation performed in Sec 3.1.2, we propose the alternative measure of anisotropy

$$r_M = \frac{\max(\delta_i) - \min(\delta_i)}{2}, \quad \text{with} \quad i = X, Y, Z, \tag{A.3}$$

where δ_i indicates the principal components of the tensor of effective transport coefficients; the capital letters X, Y, and Z indicate the principal directions.

We analyze i) the microstructures considered in Sec 3.1.2 with ellipses randomly distributed in space (insets in Fig. 3a and 3 b shows the microstructures for the two aspect ratio values considered), and ii) the microstructure considered in Sec 3.2 (described through the unit cell represented in Fig. 4). The following assumptions are made to perform the comparison:

1. We assume that the values of tortuosity provided in the references correspond to the principal directions because none of the references provide off-diagonal values.
2. Since we perform two-dimensional simulations, we assume that the effective transport coefficient is equal to 1 in the direction not considered in this study (we therefore use $\delta_z = 1$). From a three-dimensional perspective, the two-dimensional ion-transport blocking phases considered in this study are equivalent to cylinders with axes parallel to the third direction (z) and elliptic cross-sections. This assumption about the third direction is needed to evaluate the measure of anisotropy proposed by Cooper et al. [4] without modifications to Eqs. (A.1) and (A.2). We stress that by setting $\delta_z = 1$ we identify the upper bound value for σ_C, as any other choice of $\delta_z \geq \min(\delta_x, \delta_y)$ leads to smaller values of σ_C (i.e., to lower degrees of anisotropy).

The results reported in Table A.1 can be summarized as follows. With the anisotropy measure σ_C (A.1), the largest value obtained with our geometries is 2.56 (for randomly distributed ellipses with aspect ratio $a/b = 3$, Fig. 3b). This value is 20% larger than the largest value reported for electrode components (2.07, for graphite [10]) and 4.6 times smaller than the largest value reported for separators (11.8, for PP [9]). With the anisotropy measure r_M (A.3), the largest value obtained with our geometries is 0.13 (for regularly distributed ellipses with aspect ratio $a/b = 2.5$, Fig. 4). This value is 31% larger than the largest value reported for electrode components (0.09, for graphite [10]) and 46% larger than the largest value reported for separators (0.07, for PP [9]). Our geometries are definitively plausible according to the anisotropy metric proposed by Cooper et al. [4] as their values of σ_C fall within the range of real battery materials. Actually, the metric proposed in this study leads to a more severe evaluation of our own geometries and, in our opinion, this adds value to the metric proposed.

From this rough comparison, the outcomes of the metrics σ_C and r_M appear consistent, but with some differences. Both metrics agree about the identification of the most anisotropic material for electrode (graphite [10]) and separator (PP [9]) components, even if they disagree about the material that shows the highest degree of anisotropy. A desirable feature of metric r_M is that it is bounded between 0 and 1 because each component of $\boldsymbol{\delta}$ ranges between 0 and 1. This can be helpful for the classification of porous battery material as it makes comparisons immediate. Further analyses should be performed for a thorough comparison of the two metrics, but this falls beyond the scope of this study.

To conclude, we stress that r_M (A.3) quantifies the maximum possible value of the off-diagonal terms of $\boldsymbol{\delta}$ (20) for a given porous material (refer to Fig. 3c and 3 d). The last column of Table A.1 shows the ratio between the maximum value achievable by the off-diagonal term and the maximum principal effective coefficient. From this estimate, we once more conclude that the off-diagonal terms of the transport tensor are not a priori negligible for real materials used in batteries. The actual value of the

Table A.1
Transport properties and degree of anisotropy. References [5,9,10] provide porosity ϵ and three-dimensional tortuosity values in terms of τ_x, τ_y, and τ_z. Relationship (18a) is used to convert tortuosity values into effective transport coefficients and vice versa.

Component	material	ϵ	τ_x	τ_y	τ_z	δ_x	δ_y	δ_z	τ_c (A.2)	σ_C (A.1)	r_M (A.3)	$\frac{r_M}{\delta_{max}}$
electrode [5][a]	$LiMn_2O_4$	0.36	8.29	2.31	4.97	0.04	0.16	0.07	3.97	1.50	0.06	0.36
	$LiMn_2O_4$	0.38	6.50	2.22	3.96	0.06	0.17	0.01	3.50	1.22	0.06	0.33
electrode [10]	$LiCoO_2$	0.51	3.02	2.23	2.17	0.17	0.23	0.24	2.42	0.35	0.03	0.14
	graphite	0.40	6.12	1.70	1.60	0.07	0.24	0.25	2.18	2.07	0.09	0.37
separator [9]	PE	0.40	2.78	2.92	3.04	0.14	0.14	0.13	2.91	0.09	0.01	0.04
	PP	0.35	2.32	3.24	48.7	0.15	0.11	0.01	3.95	11.8	0.07	0.48
this work	Fig. 3c[b]	0.50	1.43	1.92	0.50	0.35	0.26	1.00	0.93	1.53	0.05[d]	0.13[e]
	Fig. 3d[b]	0.50	1.25	2.94	0.50	0.40	0.17	1.00	0.96	2.56	0.11[d]	0.29[e]
	Sec 3.2[c]	0.50	1.14	2.78	0.50	0.44	0.18	1.00	0.93	2.46	0.13[d]	0.30[e]

[a] The values from Ref. [5] are indicated with τ^2 therein and are consistent with relationship (18a).
[b] The values of δ_x and δ_y refer to the principal directions, with $\delta_{ij} = 0$ for $i \neq j$ according to the Mohr's circles of Fig. 3c and 3d.
[c] The microstructure considered in Sec 3.2 is such that the orientation of the ellipse is $\theta = 0^\circ$, and the effective coefficients are $\delta_{11} = \delta_{22} = 0.31$ and $\delta_{12} = \delta_{21} = 0.13$ (refer to (24)). The values of δ_x and δ_y are thus calculated as $\delta_x = 0.31 + 0.13 = 0.44$ and $\delta_y = 0.31 - 0.13 = 0.18$ for compatibility with the other geometries (refer to note b above).
[d] Calculated as $(\delta_x - \delta_y)/2$. This is consistent with the fact that a two-dimensional framework is discussed in the manuscript. As such, the third component δ_z does not play any role. In fact, the Mohr's circles shown in Fig. 3 do not take into account the contribution of the third direction. Moreover, the off-diagonal term δ_{xy}, that affects the results described in Sec 3.2, arises from the interaction between transport components in x and y directions only.
[e] Calculated as $(1 - \delta_y/\delta_x)/2$ for compatibility with the arguments in note d above.

off-diagonal terms depends on the orientation of the coordinate system with respect to the principal coordinate system (the one for which diagonal terms vanish). An estimate of the maximum achievable value is useful because the main direction of transport i) may not coincide with one of the principal axis, and ii) may coincide with one of the principal axis for the as-produced porous component, but this might not be the case for the entire battery life.

We assumed that the properties listed in Table A.1 refer to the principal directions (i.e., that they have been evaluated along the directions for which the off-diagonal terms are indeed zero). Should this not be the case, the radius of the Mohr's circle associated to them could be even larger, with a correspondingly higher maximum value of the off-diagonal terms.

Supplementary material

Supplementary material associated with this article can be found, in the online version, at doi:10.1016/j.electacta.2021.139045.

References

[1] M. Doyle, T.F. Fuller, J. Newman, Modeling of Galvanostatic charge and discharge of the lithium/polymer/insertion cell, J. Electrochem. Soc. 140 (6) (1993) 1526, doi:10.1149/1.2221597.
[2] B. Tjaden, S.J. Cooper, D.J. Brett, D. Kramer, P.R. Shearing, On the origin and application of the Bruggeman correlation for analysing transport phenomena in electrochemical systems, Curr. Opin. Chem. Eng. 12 (2016) 44–51, doi:10.1016/j.coche.2016.02.006.
[3] A. Gupta, J.H. Seo, X. Zhang, W. Du, A.M. Sastry, W. Shyy, Effective transport properties of $LiMn_2O_4$ electrode via particle-scale modeling, J. Electrochem. Soc. 158 (5) (2011) A487–A497, doi:10.1149/1.3560441.
[4] S.J. Cooper, D. Eastwood, J. Gelb, G. Damblanc, D.J.L. Brett, R.S. Bradley, P.J. Withers, P.D. Lee, A.J. Marquis, N.P. Brandon, P.R. Shearing, Image based modelling of microstructural heterogeneity in $LiFePO_4$ electrodes for Li-ion batteries, J. Power Sources 247 (2014) 1033–1039, doi:10.1016/j.jpowsour.2013.04.156.
[5] B. Tjaden, D.J.L. Brett, P.R. Shearing, Tortuosity in electrochemical devices: a review of calculation approaches, Int. Mater. Rev. 63 (2) (2018) 47–67, doi:10.1080/09506608.2016.1249995.
[6] J. Cannarella, C.B. Arnold, Ion transport restriction in mechanically strained separator membranes, J. Power Sources 226 (2013) 149–155, doi:10.1016/j.jpowsour.2012.10.093.
[7] Y.-H. Chen, C.-W. Wang, X. Zhang, A.M. Sastry, Porous cathode optimization for lithium cells: Ionic and electronic conductivity, capacity, and selection of materials, J. Power Sources 195 (9) (2010) 2851–2862, doi:10.1016/j.jpowsour.2009.11.044.
[8] W. Du, N. Xue, W. Shyy, J.R.R.A. Martins, A surrogate-based multi-scale model for mass transport and electrochemical kinetics in Lithium-ion battery electrodes, J. Electrochem. Soc. 161 (8) (2014) E3086–E3096, doi:10.1149/2.013408jes.
[9] M.F. Lagadec, R. Zahn, V. Wood, Designing polyolefin separators to minimize the impact of local compressive stresses on lithium-ion battery performance, J. Electrochem. Soc. 165 (9) (2018) A1829–A1836, doi:10.1149/2.0041809jes.
[10] M. Ebner, D.-W. Chung, R.E. García, V. Wood, Tortuosity anisotropy in lithium-ion battery electrodes, Adv. Energy Mater. 4 (5) (2014) 1301278, doi:10.1002/aenm.201301278.
[11] M.F. Lagadec, M. Ebner, R. Zahn, V. Wood, Communication—Technique for visualization and quantification of lithium-ion battery separator microstructure, J. Electrochem. Soc. 163 (6) (2016) A992–A994, doi:10.1149/2.0811606jes.
[12] M.F. Lagadec, R. Zahn, S. Müller, V. Wood, Topological and network analysis of lithium-ion battery components: the importance of pore space connectivity for cell operation, Energy Environ. Sci. 11 (11) (2018) 3194–3200, doi:10.1039/c8ee00875b.
[13] U. Pasaogullari, P.P. Mukherjee, C.-Y. Wang, K.S. Chen, Anisotropic heat and water transport in a PEFC cathode gas diffusion layer, J. Electrochem. Soc. 154 (8) (2007) B823, doi:10.1149/1.2745714.
[14] J. Tan, A.M. Tartakovsky, K. Ferris, E.M. Ryan, Investigating the effects of anisotropic mass transport on dendrite growth in high energy density Lithium batteries, J. Electrochem. Soc. 163 (2) (2015) A318–A327, doi:10.1149/2.0951602jes.
[15] V.P. Nemani, S.J. Harris, K.C. Smith, Design of bi-tortuous, anisotropic graphite anodes for fast ion-transport in Li-ion batteries, J. Electrochem. Soc. 162 (8) (2015) A1415–A1423, doi:10.1149/2.0151508jes.
[16] A. Bejan, Advanced Engineering Thermodynamics, John Wiley & Sons, Inc., 2016, doi:10.1002/9781119245964.
[17] A. Mukhopadhyay, B.W. Sheldon, Deformation and stress in electrode materials for Li-ion batteries, Progr. Mater. Sci. 63 (2014) 58–116, doi:10.1016/j.pmatsci.2014.02.001.
[18] R.E. Garciá, Y.-M. Chiang, Spatially resolved modeling of microstructurally complex battery architectures, J. Electrochem. Soc. 154 (9) (2007) A856–A864, doi:10.1149/1.2754072.
[19] G.M. Goldin, A.M. Colclasure, A.H. Wiedemann, R.J. Kee, Three-dimensional particle-resolved models of Li-ion batteries to assist the evaluation of empirical parameters in one-dimensional models, Electrochim. Acta 64 (2012) 118–129, doi:10.1016/j.electacta.2011.12.119.
[20] M.E. Ferraro, B.L. Trembacki, V.E. Brunini, D.R. Noble, S.A. Roberts, Electrode mesoscale as a collection of particles: Coupled electrochemical and mechanical analysis of NMC cathodes, J. Electrochem. Soc. 167 (1) (2020) 013543, doi:10.1149/1945-7111/ab632b.
[21] P. Arora, Z.J. Zhang, Battery separators, Chem. Rev. 104 (10) (2004) 4419–4462, doi:10.1021/cr020738u.
[22] F. Feyel, J.-L. Chaboche, FE^2 multiscale approach for modelling the elastoviscoplastic behaviour of long fibre SiC/Ti composite materials, Comput. Methods Appl. Mech. Eng. 183 (3-4) (2000) 309–330, doi:10.1016/s0045-7825(99)00224-8.
[23] C. Miehe, Strain-driven homogenization of inelastic microstructures and composites based on an incremental variational formulation, Int. J. Numer. Methods Eng. 55 (11) (2002) 1285–1322, doi:10.1002/nme.515.
[24] B.S. Mercer, K.K. Mandadapu, P. Papadopoulos, Novel formulations of microscopic boundary-value problems in continuous multiscale finite element meth-

ods, Comput. Methods Appl. Mech. Eng. 286 (2015) 268–292, doi:10.1016/j.cma.2014.12.021.
[25] A. Sengupta, P. Papadopoulos, R.L. Taylor, A multiscale finite element method for modeling fully coupled thermomechanical problems in solids, Int. J. Numer. Methods Eng. 91 (13) (2012) 1386–1405, doi:10.1002/nme.4320.
[26] J. Schröder, Derivation of the localization and homogenization conditions for electro-mechanically coupled problems, Comput. Mater. Sci. 46 (3) (2009) 595–599, doi:10.1016/j.commatsci.2009.03.035.
[27] J. Schröder, M.-A. Keip, Two-scale homogenization of electromechanically coupled boundary value problems, Comput. Mech. 50 (2) (2012) 229–244, doi:10.1007/s00466-012-0715-9.
[28] M.-A. Keip, P. Steinmann, J. Schröder, Two-scale computational homogenization of electro-elasticity at finite strains, Comput. Methods Appl. Mech. Eng. 278 (2014) 62–79, doi:10.1016/j.cma.2014.04.020.
[29] S. Lee, V. Sundararaghavan, Multi-scale modeling of moving interface problems with flux and field jumps: Application to oxidative degradation of ceramic matrix composites, Int. J. Numer. Methods Eng. 85 (6) (2010) 784–804, doi:10.1002/nme.2996.
[30] F. Fritzen, M. Hodapp, The finite element square reduced (FE2R) method with GPU acceleration: towards three-dimensional two-scale simulations, Int. J. Numer. Methods Eng. 107 (10) (2016) 853–881, doi:10.1002/nme.5188.
[31] F. Fritzen, M. Fernández, F. Larsson, On-the-fly adaptivity for nonlinear twoscale simulations using artificial neural networks and reduced order modeling, Front. Mater. 6 (2019) 75, doi:10.3389/fmats.2019.00075.
[32] A. Salvadori, E. Bosco, D. Grazioli, A computational homogenization approach for Li-ion battery cells: Part 1 – formulation, J. Mech. Phys. Solids 65 (2014) 114–137, doi:10.1016/j.jmps.2013.08.010.
[33] A. Salvadori, D. Grazioli, M.G.D. Geers, Governing equations for a two-scale analysis of Li-ion battery cells, Int. J. Solids Struct. 59 (2015) 90–109, doi:10.1016/j.ijsolstr.2015.01.014.
[34] J. Cannarella, C.B. Arnold, Stress evolution and capacity fade in constrained lithium-ion pouch cells, J. Power Sources 245 (2014) 745–751, doi:10.1016/j.jpowsour.2013.06.165.
[35] W. Du, A. Gupta, X. Zhang, A.M. Sastry, W. Shyy, Effect of cycling rate, particle size and transport properties on lithium-ion cathode performance, Int. J. Heat Mass Transf. 53 (17–18) (2010) 3552–3561, doi:10.1016/j.ijheatmasstransfer.2010.04.017.
[36] D. Perić, E.A. de Souza Neto, R.A. Feijóo, M. Partovi, A.J.C. Molina, On micro-to-macro transitions for multi-scale analysis of non-linear heterogeneous materials: unified variational basis and finite element implementation, Int. J. Numer. Methods Eng. 87 (1-5) (2010) 149–170, doi:10.1002/nme.3014.
[37] I. Özdemir, W.A.M. Brekelmans, M.G.D. Geers, Computational homogenization for heat conduction in heterogeneous solids, Int. J. Numer. Methods Eng. 73 (2) (2007) 185–204, doi:10.1002/nme.2068.
[38] R. Hill, Elastic properties of reinforced solids: Some theoretical principles, J. Mech. Phys. Solids 11 (5) (1963) 357–372, doi:10.1016/0022-5096(63)90036-x.
[39] I. Özdemir, W. Brekelmans, M. Geers, FE^2 computational homogenization for the thermo-mechanical analysis of heterogeneous solids, Comput. Methods Appl. Mech. Eng. 198 (3-4) (2008) 602–613, doi:10.1016/j.cma.2008.09.008.
[40] K. Matouš, M.G.D. Geers, V.G. Kouznetsova, A. Gillman, A review of predictive nonlinear theories for multiscale modeling of heterogeneous materials, J. Comput. Phys. 330 (2017) 192–220, doi:10.1016/j.jcp.2016.10.070.
[41] X. Zhang, D.M. Tartakovsky, Effective ion diffusion in charged nanoporous materials, J. Electrochem. Soc. 164 (4) (2017) E53–E61, doi:10.1149/2.0491704jes.
[42] D.-W. Chung, M. Ebner, D.R. Ely, V. Wood, R.E. García, Validity of the Bruggeman relation for porous electrodes, Model. Simul. Mater. Sci. Eng. 21 (7) (2013) 074009, doi:10.1088/0965-0393/21/7/074009.
[43] D.A.G. Bruggeman, Berechnung verschiedener physikalischer Konstanten von heterogenen Substanzen. I. Dielektrizitätskonstanten und Leitfähigkeiten der Mischkörper aus isotropen Substanzen, Ann. Phys. 416 (7) (1935) 636–664, doi:10.1002/andp.19354160705.
[44] L.O. Valøen, J.N. Reimers, Transport properties of $LiPF_6$-based Li-ion battery electrolytes, J. Electrochem. Soc. 152 (5) (2005) A882–A891, doi:10.1149/1.1872737.
[45] S.J. Cooper, A. Bertei, P.R. Shearing, J.A. Kilner, N.P. Brandon, TauFactor: An open-source application for calculating tortuosity factors from tomographic data, SoftwareX 5 (2016) 203–210, doi:10.1016/j.softx.2016.09.002.
[46] Z. Yan, S. Hara, N. Shikazono, Effect of powder morphology on the microstructural characteristics of $La_{0.6}Sr_{0.4}Co_{0.2}Fe_{0.8}O_3$ cathode: A kinetic Monte Carlo investigation, Int. J. Hydrog. Energy 42 (17) (2017) 12601–12614, doi:10.1016/j.ijhydene.2017.03.136.
[47] M. Ebner, V. Wood, Tool for tortuosity estimation in lithium ion battery porous electrodes, J. Electrochem. Soc. 162 (2) (2015) A3064–A3070, doi:10.1149/2.0111502jes.
[48] S.V. Erhard, P.J. Osswald, J. Wilhelm, A. Rheinfeld, S. Kosch, A. Jossen, Simulation and measurement of local potentials of modified commercial cylindrical cells, J. Electrochem. Soc. 162 (14) (2015) A2707–A2719, doi:10.1149/2.0431514jes.
[49] T. Danner, M. Singh, S. Hein, J. Kaiser, H. Hahn, A. Latz, Thick electrodes for Li-ion batteries: A model based analysis, J. Power Sources 334 (2016) 191–201, doi:10.1016/j.jpowsour.2016.09.143.
[50] T.R. Ashwin, A. McGordon, P.A. Jennings, A mass transfer based variable porosity model with particle radius change for a lithium-ion battery, Electrochim. Acta 232 (2017) 203–214, doi:10.1016/j.electacta.2017.02.129.
[51] W. Mai, M. Yang, S. Soghrati, A particle-resolved 3D finite element model to study the effect of cathode microstructure on the behavior of lithium ion batteries, Electrochim. Acta 294 (2019) 192–209, doi:10.1016/j.electacta.2018.10.072.
[52] X. Zhang, Multiscale Modeling of Li-ion Cells: Mechanics, Heat Generation and Electrochemical Kinetics, University of Michigan, 2009 Ph.D. thesis.
[53] M. Quintard, L. Bletzacker, D. Chenu, S. Whitaker, Nonlinear, multicomponent, mass transport in porous media, Chem. Eng. Sci. 61 (8) (2006) 2643–2669, doi:10.1016/j.ces.2005.11.034.
[54] M.F. Lagadec, R. Zahn, V. Wood, Characterization and performance evaluation of lithium-ion battery separators, Nat. Energy 4 (1) (2018) 16–25, doi:10.1038/s41560-018-0295-9.
[55] W.F. Hosford, Mechanical Behavior of Materials, Cambridge University Press, 2005, doi:10.1017/cbo9780511810930.
[56] C.-F. Yang, L.-J. Qin, Graphical representation and explanation of the conductivity tensor of anisotropic media, Surv. Geophys. 41 (2) (2020) 249–281, doi:10.1007/s10712-019-09581-5.
[57] Z. Yan, S. Hara, N. Shikazono, W. Negishi, A. Kajihara, Microstructure anisotropy of $La_{0.6}Sr_{0.4}Co_{0.2}Fe_{0.8}O_{3-\delta}$ film on rigid $Gd_{0.1}Ce_{0.9}O_{1.95}$ substrate during constrained sintering, J. Eur. Ceram. Soc. 39 (15) (2019) 4850–4863, doi:10.1016/j.jeurceramsoc.2019.07.004.
[58] X. Han, M. Ouyang, L. Lu, J. Li, Simplification of physics-based electrochemical model for lithium ion battery on electric vehicle. Part I: diffusion simplification and single particle model, J. Power Sources 278 (2015) 802–813, doi:10.1016/j.jpowsour.2014.12.101.
[59] P. Daubinger, F. Ebert, S. Hartmann, G.A. Giffin, Impact of electrochemical and mechanical interactions on lithium-ion battery performance investigated by Operando dilatometry, J. Power Sources 488 (2021) 229457, doi:10.1016/j.jpowsour.2021.229457.